Matter

CellPress

Review

Sputtered transparent electrodes for optoelectronic devices: Induced damage and mitigation strategies

Erkan Aydin,[1,*] Cesur Altinkaya,[1,2] Yury Smirnov,[3] Muhammad A. Yaqin,[1] Kassio P.S. Zanoni,[4] Abhyuday Paliwal,[4] Yuliar Firdaus,[1,5] Thomas G. Allen,[1] Thomas D. Anthopoulos,[1] Henk J. Bolink,[4] Monica Morales-Masis,[3] and Stefaan De Wolf[1,*]

SUMMARY

Transparent electrodes and metal contacts deposited by magnetron sputtering find applications in numerous state-of-the-art optoelectronic devices, such as solar cells and light-emitting diodes. However, the deposition of such thin films may damage underlying sensitive device layers due to plasma emission and particle impact. Inserting a buffer layer to shield against such damage is a common mitigation approach. We start this review by describing how sputtered transparent top electrodes have become archetypal for a broad range of optoelectronic devices and then discuss the possible detrimental consequences of sputter damage on device performance. Next, we review common buffer-layer materials in view of their processing-property-performance relationship. Finally, we discuss strategies to eliminate the buffer-layer requirement by implementing alternative, soft-landing deposition techniques for top electrodes. Our review highlights the critical issue of sputter damage for optoelectronic devices, formulates mitigation strategies, and provides cross-field learnings that can lead to more efficient and reliable optoelectronic devices aimed for commercialization.

INTRODUCTION

Optoelectronic devices, such as solar cells and light-emitting diodes (LEDs), are ubiquitous in modern society.[1] Such devices typically consist of a photoactive material, sandwiched between an electron transport layer (ETL) and hole transport layer (HTL), as well as two outer electrodes, of which at least the front electrode is usually highly transparent.[2] Examples of devices with such an architecture are silicon heterojunction (SHJ) solar cells,[3] thin-film silicon solar cells,[4] perovskite solar cells (PSCs),[5] organic solar cells (OSCs),[6] chalcogenide solar cells, colloidal quantum dots solar cells (QDSCs),[7] organic LEDs (OLEDs),[8] and quantum-dot LEDs (QLEDs).[9] Transparent conductive oxides (TCOs) are the most established choice as transparent electrodes, as they can simultaneously feature high optical transparency and electrical conductivity, are usually robust, and are deposited using well-established deposition techniques.[10]

For the fabrication of TCOs, magnetron sputtering is the most widespread technique both for lab-scale and commercial devices.[11–14] This vacuum-based deposition technique relies on the plasma excitation of a gas (usually Ar) that is ignited either via a direct current (DC) or radio frequency (RF) power source. The resulting

Progress and potential

Optoelectronic devices, such as solar cells and light-emitting diodes, as well as transparent electronic devices, rely on efficient light–matter interactions and usually require transparent top electrodes that are deposited onto a device layer stack. Magnetron sputtering, well established in the coating industry, is the most common technique to deposit such materials. Nevertheless, this process may result in irreversible damage to underlying sensitive layers because the deposition process involves high-energy particles and plasma emission. Several strategies are available to prevent such damage; some of these methods are common for various optoelectronic devices, while others have yet to be considered for specific applications. Taking inspiration across different research fields, we discuss how to choose adequate buffer layers for various optoelectronic devices as well as possible paths to eliminate their need via soft-landing methods for transparent electrodes.

plasma-related species bombard a target material, resulting in a transfer of particles from the target to the substrate. Sputtered TCOs offer excellent optoelectronic performance, high reproducibility, and additional functionalities (e.g., barrier properties against metal diffusion or humidity) due to the dense nature of most sputtered TCOs. However, the kinetic energy of the plasma particles, plasma emission, and processing-induced heat may harm underlying sensitive layers of the devices during the deposition.[15] Layers susceptible to sputter damage can be either the underlying charge transport layers or the active materials, where structural changes, such as the breaking of chemical bonds, may deteriorate material properties, thereby compromising device performance and stability.[16,17] Therefore, successful implementation of TCOs as top electrodes requires the minimization of sputter damage without jeopardizing film quality or throughput. As is addressed in this review, this may be accomplished either by utilizing additional thin-film layers that are resilient against sputter damage and do not incur device performance losses (here labeled as buffer layers, but also known as protective layers, interfacial layers, or blocking layers) or by finding alternative damage-free deposition techniques for TCOs.

Specifically, following a brief introduction about transparent electrodes as commonly used in optoelectronic devices, we discuss possible causes of device damage during sputter deposition of these transparent electrodes, followed by a review of materials and methods to fabricate protective buffer layers, focusing on their processing-property-performance relation and appropriateness for a given device technology. Moreover, from a performance and cost perspective, buffer-layer elimination may be desirable (as their deposition adds an additional processing step; their presence can also impose a carrier-transport barrier in contact stacks). This, however, requires process sophistication or even the replacement of magnetron sputtering by alternative soft-landing deposition techniques to fabricate these transparent electrodes. We discuss available alternative deposition methods and provide an outlook for further developing damage-free deposition of TCOs on optoelectronic devices that feature process-sensitive layers.

TRANSPARENT TOP ELECTRODE REQUIREMENTS FOR OPTOELECTRONIC DEVICES

In archetypal solar cells and top-emitting (or upwards-emitting) LEDs, an ideal transparent top electrode must effectively extract or inject charges while exhibiting minimal optical and electrical losses. Independent from the application, all transparent electrode materials should combine (1) transparency in the spectral range of absorption or emission of the device, (2) high lateral conductivity, (3) low-resistance Ohmic contact with adjacent layers, (4) chemical stability, and (5) low processing impact to the underlying layers. Specifically, TCO films capping the device layer stack as transparent electrodes may also improve protection against moisture ingress.[18] To better understand the necessity of an additional buffer layer to accomplish these criteria, this section first discusses the formation of transparent electrodes and their impact at the device level. Here, we give a nonexhaustive description of commonly used transparent electrodes with perspective of performance and robustness relation. For a detailed investigation of the optoelectronic properties of TEs, we encourage readers to check the review by Morales-Masis et al.[10]

Types of transparent electrodes

One simple approach to obtain a transparent electrode consists of thermally evaporating ultrathin (<10 nm) metallic films such as Ag, Au, or Al, which can provide a high lateral conductivity and are suitable for flexible devices;[10] however, a low

[1]KAUST Solar Center (KSC), Physical Sciences and Engineering Division (PSE), King Abdullah University of Science and Technology (KAUST), Thuwal 23955-6900, Kingdom of Saudi Arabia

[2]Department of Energy Systems Engineering, Faculty of Engineering and Natural Sciences, Ankara Yıldırım Beyazıt University, Ankara 06010, Turkey

[3]MESA+ Institute for Nanotechnology, University of Twente, Enschede 7500 AE, the Netherlands

[4]Instituto de Ciencia Molecular, Universidad de Valencia, C/Catedrático J. Beltrán 2, Paterna 46980, Spain

[5]Now at Research Center for Electronics and Telecommunication, Indonesian Institute of Science, Jalan Sangkuriang Komplek LIPI Building 20 level 4, Bandung 40135, Indonesia

*Correspondence:
erkan.aydin@kaust.edu.sa (E.A.),
stefaan.dewolf@kaust.edu.sa (S.D.W.)

https://doi.org/10.1016/j.matt.2021.09.021

percolation threshold is desirable to ensure high transparency. The percolation threshold defines the minimum material coverage (continuous network of connections between particles or wires) required to provide adequate conductivity while offering sufficient optical transparency. This value is usually high for metal films, implying that dense (continuous) films are needed to ensure a high conductivity at the expense of reduced optical transparency. Presynthesized metal nanowires (NWs) can be deposited as an alternative to metal thin films, which offer a lower percolation threshold.[19] However, metal NWs (e.g., synthesized from Ag, Cu, Au) usually exhibit poor adhesion as well as a high contact resistance with their adjacent materials and a poor chemical and environmental stability due to atmospheric corrosion driven by their large surface-to-volume ratio. A promising approach to overcome the mechanical stability issues of metal NWs is to embed them into a polymer matrix.[20] A similar approach is used for hybrid polymer/carbon-nanomaterials as transparent electrodes.[21] In this sense, carbon-based materials, such as carbon nanotubes (CNTs) and graphene, have gained much interest as stand-alone transparent electrodes due to their excellent electrical properties, combined with high flexibility and chemical stability, as well the potential to deposit such layers using simple processing techniques (such as ink-jet printing). Nevertheless, even though some hybrid transparent electrodes based on Ag-NW/CNT have reached the requirements for the anodes of efficient OLED displays, the scaled processing of carbon-based transparent electrodes over large areas is yet to be demonstrated.[10,22]

Sandwiching thin metal films (Ag, Au, Cu with $\leq$10 nm in thickness) into dielectric metal oxides (WO_x, V_2O_x, MoO_x) is another hybrid approach with attractive properties for certain applications; such dielectric/metal/dielectric (DMD) multilayer structures have yielded decent transparency ($\geq$70%) and conductivity characteristics close to conventional TCOs.[23–27] DMD electrodes provide better elasticity than crystalline TCO electrodes (e.g., indium tin oxide [ITO]) due to the good flexibility of intermediate metal layers, making these electrodes advantageous to utilize in flexible optoelectronics. The requirement of delicate thickness control over the layers to achieve optimum transparency, as well as the stability issues of metal films (Cu, Ag) and their high cost (Au, Ag; need for multiple depositions) are concerns yet to be solved for DMD electrodes. To learn more about DMD electrodes, we also encourage readers to consult previously published reviews by Cao et al.,[28] and Kim and Lee.[23]

As an alternative to these approaches, conductive polymers can be employed as low-cost and flexible transparent electrodes. However, to date, poly(3,4-ethylenedioxythiophene) (PEDOT) is the only state-of-the-art transparent conducting polymer with suitable conductivities to serve as an electrode.[22,29] This conjugated polymer can be doped by partial oxidation of the thiophene in the liquid or vapor phase. The former is commonly done in the presence of poly(styrene sulfonate) (PSS), acting as the counter ion and stabilizer for the doped PEDOT. However, the hygroscopic and corrosive nature of PEDOT:PSS might cause device degradation under operation, hence a short life span.[30,31] Nevertheless, utilizing oxidative chemical vapor deposition (oCVD) followed by acid treatment can give highly conductive (6259 S/cm) and air-stable PEDOT films.[32]

Despite the development of these alternative approaches in the lab environment, most of the state-of-the-art solar cells and top-emitting organic/QD LEDs for commercial applications rely on the deposition of TCOs as transparent electrodes at the final stage of device processing. Critical advantages of TCOs are their well-established deposition methods with high throughput, high stability, and, critically, high electrical mobility

Table 1. Comparison of transparent electrodes for various optoelectronic devices

Materials	Device applications	Deposition methods	Benefits	Drawbacks
TCOs	silicon and thin-film solar cells , PSCs, OSCs, LEDs	sputtering, PLD[a], CVD[b], ALD[c], solution processing	low resistivity and high transparency, well-established fabrication, excellent thermal and chemical stability	expensive, sputtered TCOs: damage to layers underneath, in-based TCOs: the scarcity of indium
carbon nanotubes	PSCs, OSCs	solution transfer, CVD	high conductivity and transparency, low cost	expensive, limited dispersibility, low conductivity, poor stability
graphene sheets	PSCs	CVD, thin film transfer techniques	high conductivity and transparency	low work function, poor doping stability, uniformity over large areas
thin metal films	LEDs, OSCs	evaporation, sputtering	simple process	trade-off between conductivity and transparency, poor stability, sputtered: damage to layers underneath
metal nanowires	PSCs, OSCs	solution processing	good conductivity	high roughness, poor adhesion, high contact resistance
dielectric/metal/dielectric multilayers	PSCs, OSCs, LEDs	Evaporation	good conductivity, transparency, and high mechanical flexibility	demanding precise thickness control of the multilayer stack, possible low stability due to metal interlayer films
conductive polymers	OSCs, LEDs	solution processing, CVD	low cost, flexible conductors	hygroscopic nature, poor stability

[a]Pulsed laser deposition.
[b]Chemical vapor deposition.
[c]Atomic layer deposition.

coupled with high transparency. TCOs with especially high carrier mobilities include those based primarily on indium oxide, similar to the archetypical TCO ITO; emerging high carrier mobility TCOs in this category are hydrogen-doped indium oxide (IO:H), tungsten-doped indium oxide (IWO), and Zr-doped indium oxide (IZRO).[11–14] Most of these TCOs are polycrystalline, even though certain variants such as indium zinc oxide (IZO) are amorphous, with excellent optoelectronic properties and outstanding temperature resilience.[33] For all listed TCOs, the most common deposition technique is sputtering. However, sputtering TCOs on top of the photoactive and other functional layers may set physical and chemical limitations, as discussed in the following section. Due to the widespread use of sputtered TCOs and metal oxides and the known challenges regarding sputtering damage, we focus the rest of the section on sputter deposition of TCOs. The comparison between the discussed alternative transparent electrodes is summarized in Table 1.

Origins of damage during magnetron sputtering of TCOs

To identify the root causes of damage incurred by TCO sputtering onto sensitive layers, the working mechanism of the sputtering process should be understood. Elaborate descriptions of sputtering processes can be found in dedicated literature;[34–37] here we briefly summarize the main principles of the deposition method with relevance to damage during sputtering. Sputtering is a nonthermal, plasma-assisted physical vapor deposition (PVD) method that involves ejecting atoms or molecules from a bulk target material (cathode) onto a substrate (anode) by momentum transfer, caused by the bombardment of plasma-excited high-energy particles (usually Ar ions). This process is typically performed in a low-pressure (<5 mammalian target of rapamycin) environment, where the sputtered particles suffer negligible gas-phase collisions. The ejected material is then directed onto a substrate to form a thin film, as sketched in Figure 1. In magnetron sputtering, the plasma discharge is sustained in close vicinity of the target by magnetic confinement of the electrons. In contrast to the electrons, the ejected ions and neutral particles are barely influenced by the magnetic field.[19]

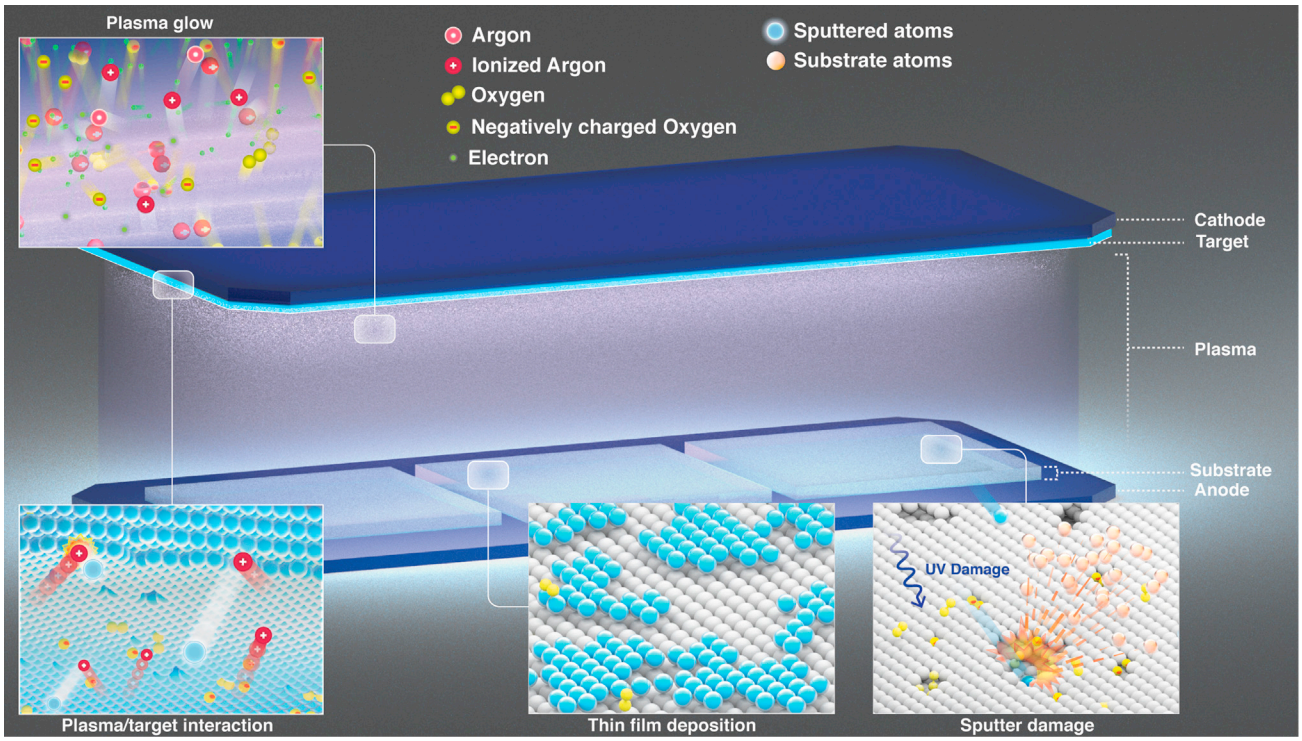

Figure 1. Sputtering process

Illustration of the sputtering process and possible damage mechanisms of the underlying substrate. The sketch explains four main physical phenomena occurring during the sputter deposition of oxide films: i.e., plasma excitation, plasma/target interaction, thin-film deposition, and sputter damage due to ion bombardment.

The discharge voltages during sputtering typically range between −200 and −800 V and will depend on the desired process conditions and specific configuration of the sputtering system. Usually, RF sputtering requires lower discharge voltages than DC sputtering (deposition by both DC and RF plasma excitation is possible for conductive materials, such as TCOs). Notably, the magnitude of the discharge voltage is linked to the level of the sputtering damage, where the application of RF sputtering might help minimize this damage.[36,38]

Sputter damage during TCO deposition is commonly attributed to the substrate's bombardment by highly energetic species. An elaborate discussion of the influence of ion bombardment on the electrical and structural properties of TCOs is given in a dedicated review by Ellmer and Welzel.[34] Here, we provide a nonexhaustive description of the main species involved in the process and the representative energies they can acquire from the following references:[34,39]

- Sputtered atoms (ions) from the target surface (~10 eV), the formation of which mainly depends on the binding energy of the target material;
- Negative ions (originating from the carrier gas) formed in the plasma (~5–15 eV), the formation of which mainly depends on the plasma potential;
- Negative ions formed at the target surface (up to 400 eV), the formation of which mainly depends on the target voltage;
- Positive ions formed in the plasma (~15 eV), the formation of which mainly depends on the potential fall in front of a substrate at floating potential;

- Reflected atoms and neutralized ions from the target surface (20–50 eV), the formation of which mainly depends on the background gas and the mass of the sputtered element.

As seen in the list above, negative ions (e.g., O^- and In^- for ITO sputtering) formed at the target surface and accelerated toward the substrate acquire the largest energy, which is determined by the potential between target and plasma potentials. Although the flux of the energetic particles is an important parameter, it was reported that high-energy negative O^- ions are additionally the most abundant species in plasma in case of reactive deposition of oxides.[34,35,40,41] However, energies of other ions/atoms (e.g., Ar^+,Ar^0, or In^0) in the discharge may already be sufficient to dissociate surface bonds or etch soft layers in certain device technologies,[39,42–46] for example, perovskite films (with Pb and I bonding energies of 2.77 and 1.58 eV, respectively),[45] organic compounds (with C-C, C-O, C-H, and C=C bonding energies of 3.7, 3.5, 3.4, and 6.2 eV, respectively),[43] as well as hydrogen bonded to crystalline silicon surfaces or within an amorphous silicon matrix (bonding energies of 3.25 eV).[46] In addition, the momentum transfer of high-energy particles from the plasma (Ar, oxygen ions) or sputtered from the target might impinge or even increase the substrate temperature sufficiently to trigger physical (e.g., etching) or thermal degradation of sensitive substrate layers. This can affect the functional properties of underlying charge transport and passivation layers and photoactive absorbers or emitters, eroding device performance. For instance, due to sputter damage, there may be inevitable interfacial consequences such as pinning of the Fermi level, caused by damage-related interface gap states, resulting in the formation of Schottky-barrier impeding carrier transport. Sputter damage can also impair the doping efficiency of materials and the lifetime of excess charge carriers in photoactive materials; in some cases, depending on its extent, such damage can even lead to a reduced shunt resistance.[47] The following sections discuss these consequences on the behaviors of typical optoelectronic devices.

Impact of sputter damage on optoelectronic devices

Solar cells

Thin-film solar cells can be fabricated in either substrate or superstrate configuration. In the *superstrate* configuration, light enters the device through the glass onto which a TCO is deposited, followed by the other device layers, such as the absorber layer (sandwiched between the ETL and HTL), and back contact (either a metal or another TCO in case of semitransparent devices or tandem solar cells). In the *substrate* configuration, the TCO is deposited onto the top charge-selective layer since light enters the device from the layer-stack side, giving freedom to choose a large variety of substrates such as flexible metal foils. In all cases when the TCO needs to be deposited on top of active device layers, damage may be induced, which must be mitigated.

Since typical state-of-the-art devices feature sensitive layers (see examples in Figure 2), sputter damage is practically unavoidable, motivating the search for adequate buffer layers (discussed in the section "buffer layers in optoelectronic devices") or strategies that can undo the damage. For example, in SHJ solar cells, the intrinsic and doped hydrogenated amorphous silicon (a-Si:H) layers that act as passivating and carrier-selective contacts on c-Si wafers are sensitive to sputter damage.[15] Here, the incurred damage can be annealed away without needing an additional buffer layer, which typically occurs during the final metal curing step. For thin-film solar cells in the substrate configuration, such as those based on $Cu_2ZnSn(S,Se)_4$ (CZTSSe), $Cu(In_xGa_{1-x})Se_2$ (CIGS), and CdTe absorbers, a buffer layer (usually *n*-type) is crucial not only to form

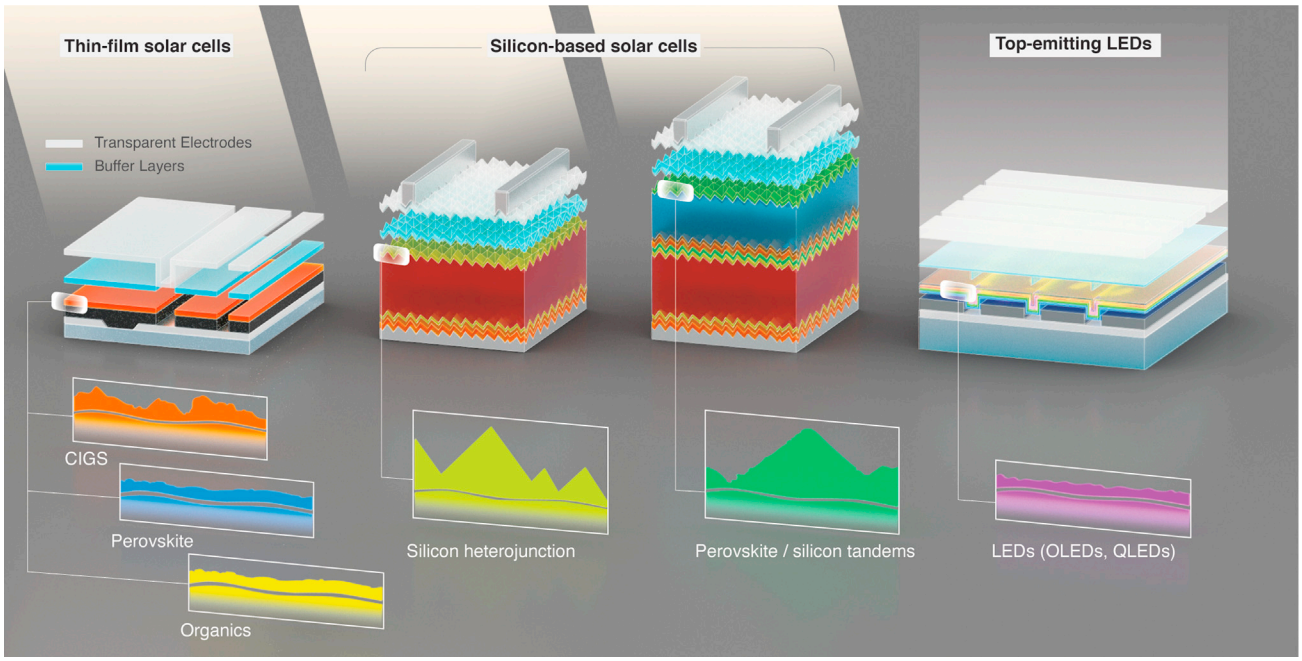

Figure 2. Device sketches of different solar cell technologies and their surface morphologies
Here, transparent electrodes and buffer layers follow the surface morphology of the underlying layers, one of the critical parameters for the deposition method selection of both the buffer layer and transparent electrode.

favorable band alignments, needed for electron extraction,[48,49] but also to protect the *p*-type absorber from sputter damage. Integrating PSCs in tandem devices such as the perovskite/silicon and perovskite/CIGS implementations has recently become a very active field of research. Such devices, aimed at very high performance photovoltaics, also require the use of TCO layers, often on both sides of the device, as well as in the recombination junction that electrically and optically couples the top and bottom cells (Figure 2).[50–53]

Suppose solar cells are not protected from sputter damage. In that case, the devices usually show S-shaped current density-voltage (*J-V*) characteristics, as shown in Figure 3.[16,54] Such devices exhibit reduced fill factors (*FF*), open-circuit voltage (V_{OC}), and short-circuit current density (J_{SC}) values, leading to low maximum power point (MPP) values. However, the observed S-shape often cannot be simply explained by suboptimal series and shunt resistances. For each type of solar cell, the source and the consequences of the damage may vary significantly.

For PSCs involving TCOs sputtered on the device stack, numerical simulations using equivalent circuit models suggest that the main reason for the observed S-shaped *J-V* curves is the formation of a Schottky diode at the TCO/HTL interface, where the sputtering process is performed (Figures 3A–3C). For example, in regular, semitransparent *n-i-p* devices (where the HTL [*p*-layer] is deposited onto the perovskite [*i*]), S-shape curves have been attributed to structural changes in spiro-OMeTAD, which is a widely used HTL, and an increase in the Schottky barrier at the TCO/spiro-OMeTAD interface upon TCO sputtering.[16] If no buffer layer is used, increasing the processing time (Figure 3C) and sputter power (Figure 3D) results in more pronounced S-shaped *J-V* curves, and thus lower MPP values.[12,16] Here, a common mitigation approach is the insertion of evaporated MoO_x (featuring good optical transparency and a high work function) as a buffer layer between the TCO and spiro-OMeTAD.[12] For the inverted *p-i-n*

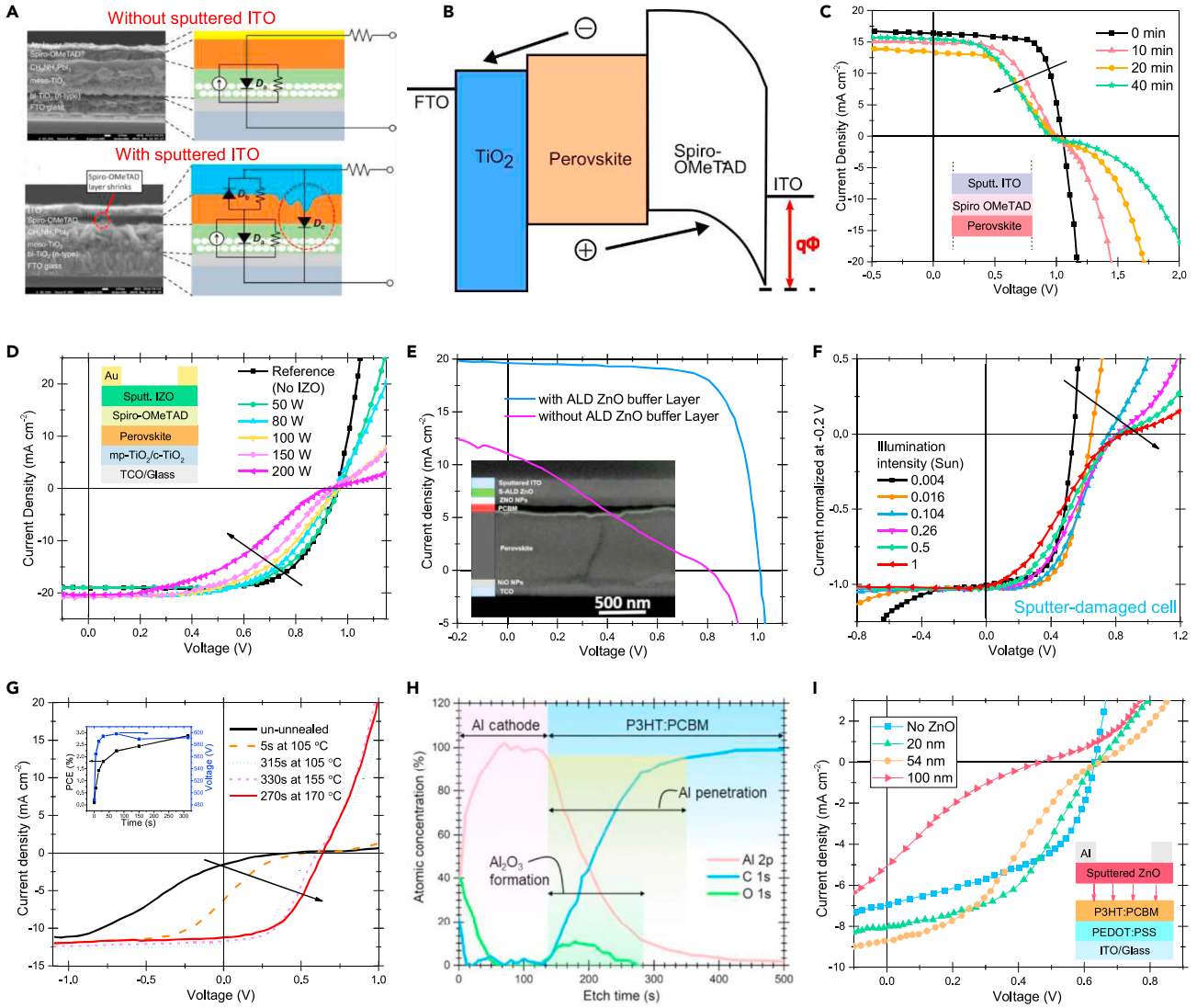

Figure 3. Sputter damage in perovskite and organic solar cells

(A) Cross-sectional scanning electron microscopy images and corresponding schematic representation of equivalent circuit model between layers of PSCs with and without sputtered ITO layer.

(B) Band diagram of corresponding PSCs showing the Schottky junction formed between spiro-OMeTAD and sputtered ITO.

(C) Current density-voltage of characteristics for increasing sputtering time of ITO layer in PSCs. The arrow indicates the direction of increasing sputtering time, and the inset shows the corresponding device structure. Reprinted with permission from Kanda et al.[16] Copyright 2016, American Chemical Society.

(D) Current density-voltage curves of *n-i-p* PSCs without buffer layer show the S-shape formation regarding increasing sputtering power of IZO layer deposition. The arrow indicates the direction of increasing sputtering power, and the inset shows the schematic device structure used for measurements. Adapted from Werner et al.[12]

(E) Current density-voltage characteristics of *p-i-n* PSCs with and without a spatially atomic layer deposited ZnO buffer layer. The inset is the SEM image of the corresponding devices. Reprinted with permission from Najafi et al.[55] Copyright 2018, Wiley-VCH.

(F) The change in current-voltage characteristics with varying illumination intensities from 0.004 to 1 sun (normalized at −0.2 V) for a cell with an IZO layer sputtered at 150 W. The arrow indicates the direction of increasing illumination intensity, and the device structure used for measurements is the same as in (D). Adapted from Werner et al.[12]

(G) Current density-voltage curves of OSCs with sputtered Al contacts for different annealing times and temperatures. The arrow indicates the direction of increasing annealing temperature and time. The insets show the evolution of PCE and V_{OC} compared with annealing time (annealed at 105°C) for devices. Adapted from Ahlswede et al.[56]

Figure 3. *Continued*

(H) An x-ray photoelectron spectroscopy depth profile of a P3HT: PCBM film covered with 100 nm of aluminum by sputtering with a target power of 1500 W, demonstrating aluminum (pink), carbon (blue), and oxygen (green). Adapted from Griffith et al.[47]

(I) Current density-voltage curves of transparent OSCs without RF magnetron sputtered the ZnO cathode interfacial layer in different thicknesses. The inset shows the device structure used for measurements. Adapted from Jouane et al.[57]

configuration (where now the HTL is deposited before the perovskite), the frequently used ETLs (e.g., C_{60} and derivatives) are also sensitive to sputter damage, again requiring a buffer layer, e.g., ZnO or SnO_x (featuring again good transparency but now a *low* work function) (Figure 3E).[55,58] For sputter-damaged devices, temperature-dependent *J-V* measurements can be useful to identify the formation of a Schottky barrier at the interfaces and quantify the barrier height. Light intensity-based *J-V* measurements can give hints about the presence of sputter damage, as at higher light intensities, the S-shaped behavior becomes more prominent (Figure 3F).[12] Also, surface-sensitive UV photoelectron spectroscopy (UPS) might provide insight into changes in energy levels due to sputtering damage.

Semiconducting polymers such as poly(3-hexylthiophene) (P3HT) are frequently studied in OSCs, which can also be damaged by metal-electrode sputtering. Indeed, highly energetic metal atoms may break the chemical bonds in the polymer, affecting its conjugation length and reducing the charge mobilities.[56] Fortunately, this deterioration can be partially recovered by post-annealing (Figure 3G), similar to SHJ solar cells. Nevertheless, metal sputtering on soft organic layers may also result in metallic current paths since highly energetic negative ions can penetrate the layers. For instance, aluminum sputtering on the P3HT:phenyl-C61-butyric acid methyl ester (PCBM) layers without buffer layers results in the penetration of aluminum atoms up to 8 nm into the organic layers and the formation of highly insulating aluminum oxide (Al_2O_x) at the interface between the aluminum electrode and the organic film, especially for higher sputtering powers (Figure 3H).[47] As another example, sputtering ZnO as a cathode interfacial layer on the photoactive layer of *p-i-n* OSCs changes the photoactive layer/ZnO interface morphology, which results in a high Schottky barrier and consequently in S-shaped *J-V* curves (Figure 3I).[57] Such damage can be irreversible. Due to the reasons mentioned above, sputtered top electrodes have not yet been fully explored in OSCs; instead, thermally evaporated thin metallic films are frequently used as transparent top electrodes. Nevertheless, the recent advances in the power conversion efficiency (PCE) of semitransparent OSCs (having increased to 12%) has been achieved at the cost of low average visible light transmittance (~19%), urging for the development of better transparent electrodes.[59]

As already alluded to, in SHJ solar cells, degradation of the a-Si:H/c-Si interface is commonly observed after the TCO deposition (Figures 4A–4C).[15,60] This process might be critical also for perovskite/silicon tandem solar cells since the recombination layer and charge-selective contact depositions required for the bottom contact of the perovskite top cell might necessitate a sputtering process on top of the SHJ bottom cell.[61] The damage, as evidenced by a loss in surface passivation quality of the SHJ cell, is a result of the formation of Si dangling bonds at the a-Si:H/c-Si interface.[15] Fortunately, this degradation can be recovered by annealing, as stated, usually during metal-paste curing of the grid electrode of the devices (Figure 4B). The cause of the damage is at least in part from plasma emission, as evidenced by employing samples covered by glass or quartz during the sputtering process, resulting in a persistent decrease in passivation quality (Figures 4A and 4C). Such sputter damage to the contact-layer/absorber interface has also been shown to adversely impact the *FF*, mainly due to the decrease in excess charge carrier lifetime at the

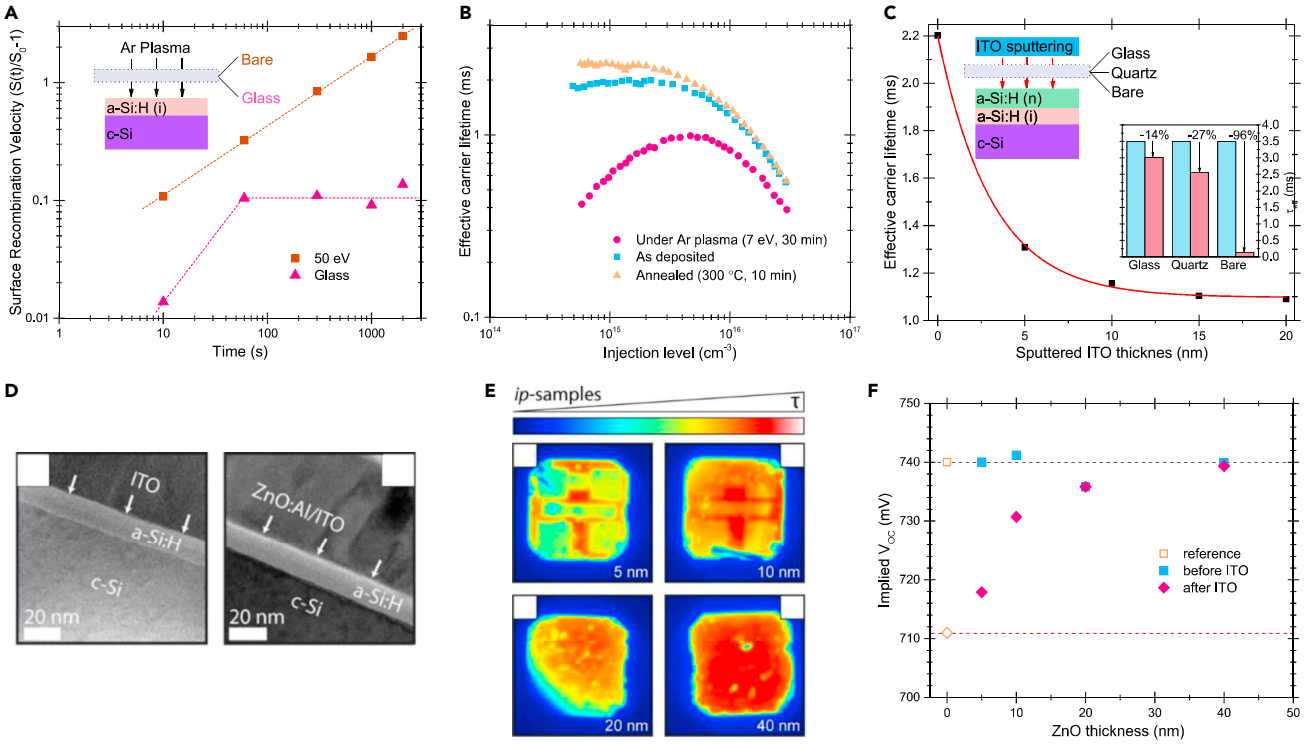

Figure 4. Sputtering damage and buffer layers in silicon heterojunction solar cells

(A) Variation in the value of surface recombination velocity for a-Si:H passivated c-Si wafers covered by the glass while exposed to Ar plasma, without any external biasing, and biased with a voltage of −50 eV without glass. The inset shows the schematic cell structure and Ar plasma application with or without glass protection.

(B) The change in effective carrier lifetime value for as-deposited a-Si:H film on c-Si wafers after Ar ion bombardment and thermal annealing. Adapted from Illiberi et al.[60]

(C) The variation of effective carrier lifetime of an n-type wafer with a-Si:H layers measured as a function of sputtered ITO thickness with corresponding device architecture used in measurements. The insets demonstrate the device architecture used in measurements and effective carrier lifetime of a wafer passivated with a-Si:H in the as-deposited state and after sputtering both when left bare and when protected by glass or quartz (the percentages indicate relative losses in a lifetime). Adapted from Demaurex et al.[15]

(D) Transmission electron microscopy images of silicon heterojunction solar cells without and with atomic layer deposited Al-doped ZnO (5 nm) buffer layers.

(E) Photoluminescence images of cells (shown in D) after ITO deposition by sputtering with varying thicknesses of the atomic layer deposited Al-doped ZnO from 5 to 40 nm.

(F) The change in implied V_{OC} values before and after ITO deposition for the samples shown in (D). The black and red dashed lines depict the value of devices before and after ITO deposition without atomic layer deposited Al-doped ZnO (the orange open-data points). Reprinted with permission from Demaurex et al.[63] Copyright 2014, IEEE.

MPP (i.e., via injection-dependent recombination), but possible also because of interfacial Fermi-level pinning effects, inducing Schottky barriers. Despite the fact that post-annealing can recover most, if not all, of the interface passivation electronically, infrared spectroscopy indicates that the a-Si:H contact layers can be structurally permanently damaged following overlayer sputtering.[15] It may thus be beneficial to insert a buffer layer to avoid such damage. Implementing thin atomic layer deposition (ALD) ZnO films in between the sputtered TCO and a-Si:H stacks may serve that function (see Figures 4D–4F), even though it was found these layers may act as a resistive interlayer, undesirably increasing the contact resistance, and thus mandating further process optimization.[62,63]

Similarly, for Cu(In, Ga)Se_2 devices, direct sputtering of TCOs onto CIGS absorbers results in a high resistance at their interfaces, as quantified by the constant phase element (CPE, which is a capacitance-like element) measured via impedance

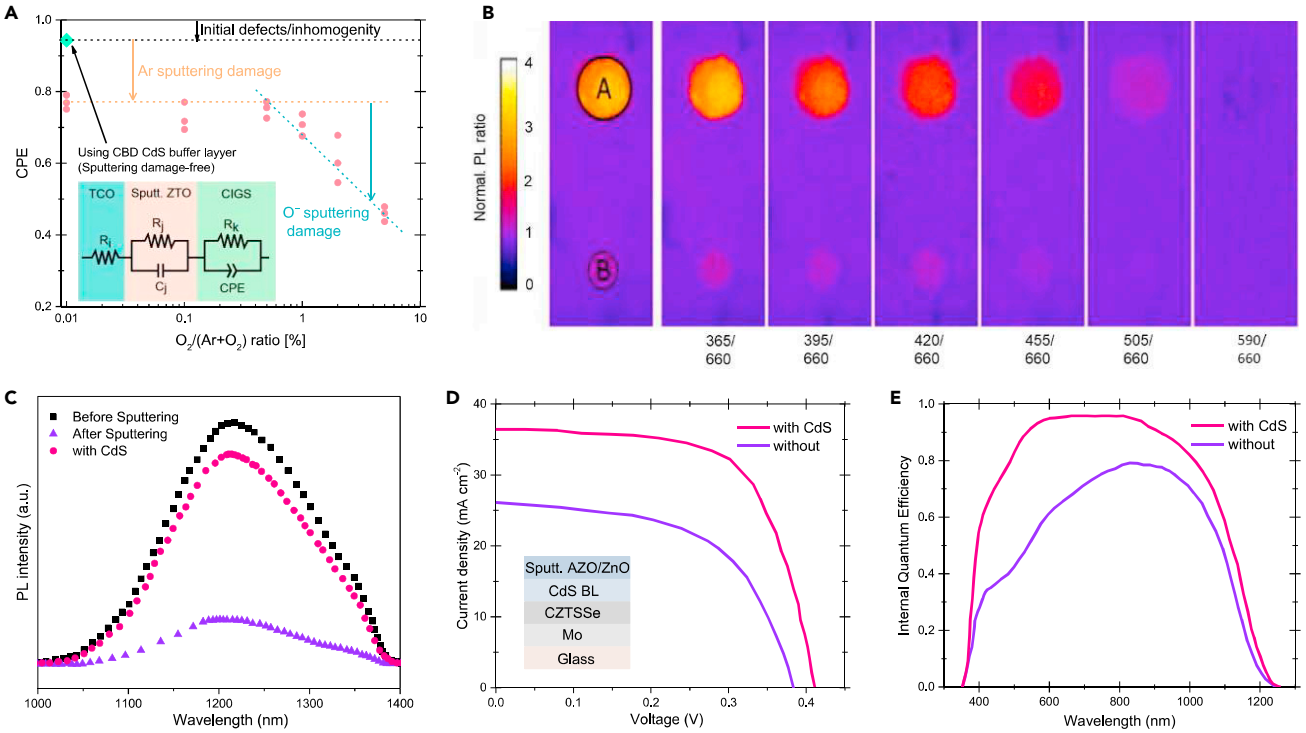

Figure 5. Sputtering damage and buffer layers in CZTSSe and CIGS solar cells

(A) Constant phase element of CIGS solar cells as a function of the oxygen partial pressure during RF sputtering of the ZTO layer. The inset shows the proposed equivalent circuit model of the CIGS solar cells for impedance spectroscopy measurement. Adapted from Sugiyama et al.[64]

(B) Normalized photoluminescence intensity ratio images in different excitation wavelengths for a CdS/CIGS/Mo sample. The A and B display intentionally thinned down zones of the CdS layer by acidic etching. The ratio images are normalized using the un-etched part of the sample as a reference. Reprinted with permission from Rey et al.[65] Copyright 2020, IEEE.

(C) Photoluminescence intensity of CZTSSe devices with and without CdS buffer layer before and after AZO/ZnO sputtering.

(D) Current density-voltage characteristics for devices with and without CdS buffer layer upon AZO/ZnO sputtering. The inset depicts the device structure employed for measurements in (C) to (E).

(E) Internal quantum efficiency curves of CZTSSe devices with and without CdS buffer layer upon AZO/ZnO sputtering. Adapted from Matsuo et al.[48]

spectroscopy (Figure 5A).[64] With increasing oxygen partial pressure in the sputtering process, thereby increasing the density of plasma species, the CPE diverges substantially from the ideal case (CPE = 1), indicating the formation of trap-state defects at the related interface hampers charge transport at the top contact. Photoluminescence (PL) intensity maps of the CdS/CIGS/Mo (top to down) for various thicknesses of the cadmium sulfide (CdS) layer show that specific thicknesses are needed for adequate protection (Figure 5B), which is discussed in detail in the section "buffer layers in optoelectronic devices."[65] As for the other types of thin-film solar cells, sputter damage usually causes quenching of the PL signal, and the device performance is deteriorated, as exemplified for CZTSSe films in Figures 5C and 5D.[48,66] This damage is usually attributed mainly to bulk defects and disorder and is responsible for a high V_{OC} deficit ($E_g/q - V_{OC}$, where E_g is the bandgap of the material and q is the electron charge) of the devices.[67]

Generally, monitoring the level of the damage is important. For this, several alternative techniques to those already mentioned can be considered, such as illuminated lock-in thermography and forward- and reverse-bias dark lock-in thermography techniques for probing the breakdown sites where current flows through weak diodes, shunts, and defects.[68] Fast determination of the carrier lifetime for perovskite absorbers is challenging due to the shorter carrier lifetimes of the perovskite films

(within nanosecond scales, resulting from its direct bandgap nature) compared with crystalline silicon (up millisecond scale, resulting from its indirect bandgap nature), thereby necessitating the use of time-resolved PL measurements, which usually take several hours.[69] Meanwhile, steady-state PL can be used for fast monitoring of the sputtering damage, as damaged layers show reduced PL peak intensity, as discussed above. Also, for large-area imaging, hyperspectral luminescence imaging can give quantifiable outputs for the carrier recombination induced by defects via the contrast on the PL or EL signal counts.[70] In addition, X-ray photoelectron spectroscopy (XPS) can be a versatile tool to monitor the chemical and electronic changes in soft layers underneath the sputtered TCOs or the sputtered TCOs themselves.[71,72] XPS helps to observe the broken chemical bonds of the organic layers upon Ar irradiation,[73] Ar implantation from sputter gas into the growing film,[74] formations of additional layers at the interface of organic films/sputtered TCOs at high sputtering powers.[75] Also, utilizing the UPS, changes in Fermi level at the substrate surface due to the oxygen implantation from the plasma were detected,[74] showing the undesired outcomes of sputtering. All these techniques provide detailed information about the sputtering damage on the layers, whereas *J-V* scans can give information about the overall device behavior. These techniques are well-established for conventional solar cell development and could be adopted by the PSC and OSC communities for faster diagnosis of process-induced damage and feedback for device development.

Light-emitting diodes

Top-emitting and transparent LEDs are essential for making active-matrix displays having high-resolution and see-through displays. Standard OLEDs are mostly vacuum-processed, usually in the *n-i-p* configuration in which light is emitted from the electron-injecting (*n*) contact. Thus, the implementation of TCOs (that have work functions >4 eV) as top electrodes in transparent OLEDs (the same in QLEDs) requires the use of low work function buffer layers (preferably vapor deposited) at the TCO/organic interface for efficient injection of electrons into the device at relatively low operational voltages.

OLEDs with sputtered metal electrodes show an undesired high leakage current in their *J-V* curves (Figure 6A), and degradation of underlying materials by sputtering is evident, as demonstrated by optical and scanning electron microscope (SEM) images in Figure 6B.[76] As discussed above, PL quenching tests are helpful for solar cells, eliminating the need for complete device fabrication to make the appropriate diagnosis. A systematic experiment using this strategy, such as exposing the aluminum (III) bis(2-methyl-8-quninolinato)-4-phenylphenolate (BAlq) respectively to an Ar ion beam (AIB), oxygen ion beam (OIB), electron beam (EB), and UV light, has revealed that the oxygen ions from the sputtering plasma are the root cause of the sputter damage.[77] The damage caused by the oxygen species is evident from the PL intensity of BAlq films after exposure to an oxygen plasma. From quenched PL values of $BAlq_3$ films, the magnitude of the damage can be ordered as UV < electrons < Ar ions < oxygen ions, as shown in Figure 6C. Increasing the sputtering power will increase the energy carried by the particles and cause more damage to soft layers (Figure 6D). Then, the damage level is also scaled with longer processing times. Excessive damage can lead to completely shorted devices, especially when the soft underlayers are very thin, either via particles with high kinetic energy or the long exposure time.

Also, organic tris(8-hydroxyquinoline)aluminum(III), Alq_3 (an electron-transport and emitting material widely used in LEDs) irradiated with 100 eV Ar^+ ions from a UV

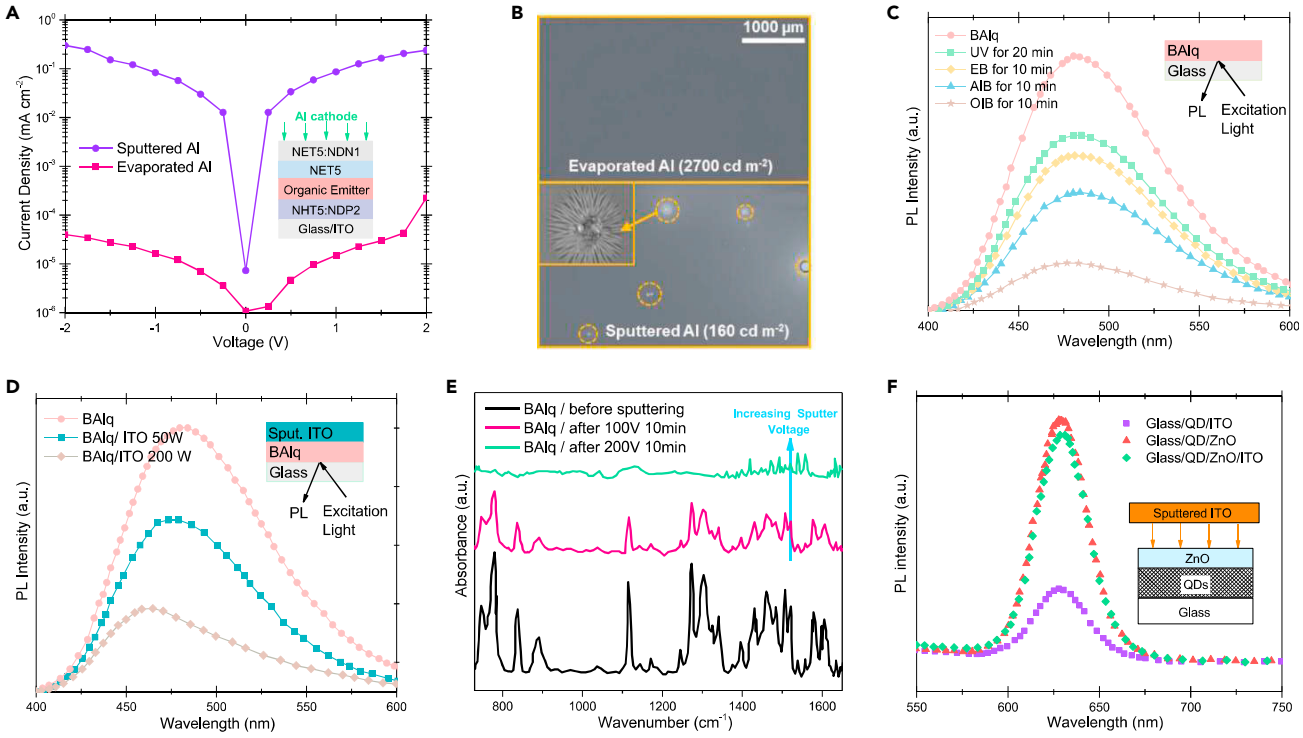

Figure 6. Sputtering damage in LEDs

(A) Current density-voltage curve of OLEDs with evaporated and sputtered Al cathodes showing the increased leakage current upon Al sputtering. The inset represents the corresponding device structure.

(B) Optical images of OLED surfaces having evaporated (luminance: 2,700 cd m^{-2}) and sputtered (luminance: 160 cd m^{-2}) Al cathodes after operation at 3 V. The inset in the optical image of a sputtered Al cathode is an SEM image of bright spots showing the degradation of sputtered Al after current-voltage-luminance measurement. Reprinted with permission from Gil et al.[76] Copyright 2009, Elsevier Inc.

(C) Photoluminescence spectra of BAlq organic film after AIB, OIB, and EB bombardment, and UV radiation. Adapted from Lei et al.[77]

(D) Photoluminescence spectra of BAlq film before and after ITO sputtering with increasing operation power. Adapted from Lei et al.[78]

(E) Fourier transform infrared spectroscopy of BAlq organic layers before and after oxygen ion bombardment at different voltages (100 V and 200 V). Adapted from Lei et al.[77]

(F) Photoluminescence spectra of colloidal CdSe/CdS/ZnS QDs with and without sputtered ITO and ZnO buffer layer. The inset depicts the device configuration used for measurements. Adapted from Wang et al.[79]

beam, shows broken bonds of Alq_3 (N-Al, C-O-Al) as revealed from peak broadening of XPS spectra and shifting in the core spectra of Al, O, N, and C.[73] For transport layers like BAlq, a very similar compound to Alq_3, the peak intensity reduction of the Fourier transform infrared spectroscopy (FT-IR) spectra after oxygen ion bombardments can also give an idea for the level of the induced damage. Figure 6E shows that oxygen ions with high energy not only induce considerable damage but also may cause a chemical reaction between oxygen ions and the BAlq film.[77] Similar to OLEDs, QLEDs are highly sensitive to sputter damage, necessitating the use of buffer layers, as depicted in Figure 6F.[79,80] CdSe/CdS/ZnS QD films exhibit relatively weak PL response under ITO sputtering, which verifies the induced damage; however, using a ZnO buffer layer alleviates the effects of the sputtering process.[79]

BUFFER LAYERS IN OPTOELECTRONIC DEVICES

To fully utilize the merits of the sputtered TCOs, implementing an additional protection layer is the state-of-the-art solution to prevent the formation or mitigate the extent of sputter damage for various optoelectronic devices (as sketched in Figure 2). Regardless of the device application, a suitable buffer layer should satisfy the

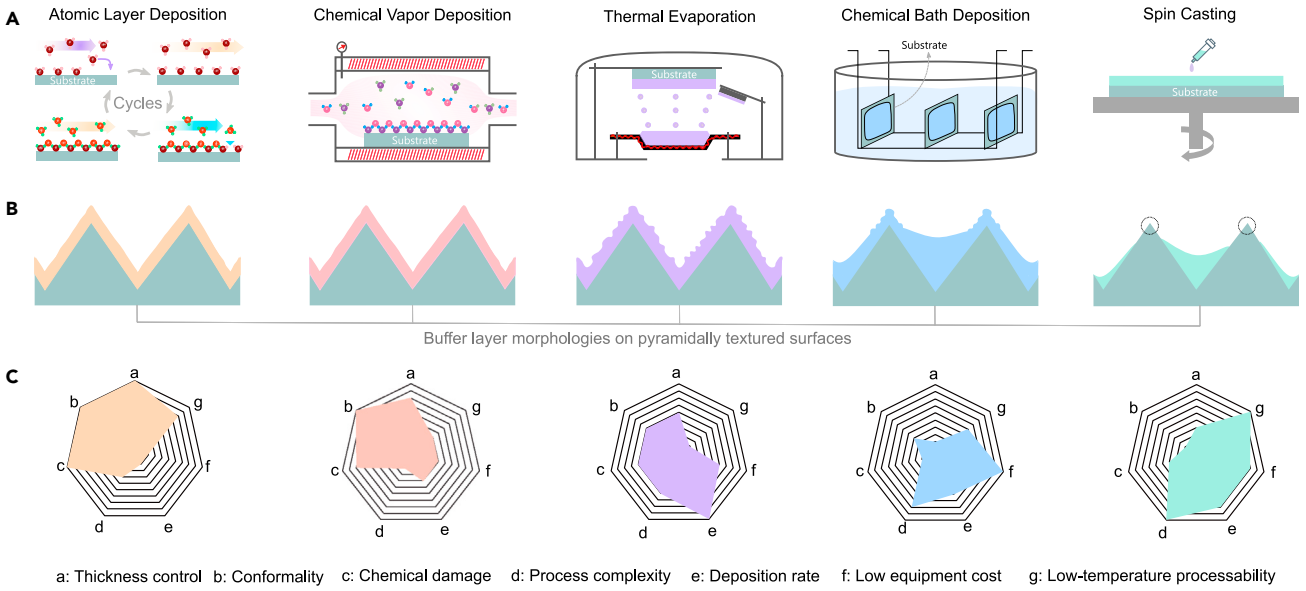

Figure 7. Various buffer-layer deposition techniques

(A) Sketches of the commonly used buffer-layer deposition techniques.

(B) Morphologies on pyramidal textured silicon surfaces of different deposition technologies. Here the textured surfaces are chosen as the representative of the most complex surfaces.

(C) The direct comparison of the deposition techniques with a spider chart.

following criteria: (1) well-matched energy alignment with the adjacent materials for efficient charge transport, (2) wide bandgap for high optical transmission, (3) an excellent refractive index match with the adjacent transparent electrode for minimized reflection (this can be verified by optical simulations),[26,81] (4) chemical inertness against underlying materials, (5) high uniformity and density of thin films (typically 5–60 nm), (6) act as a diffusion barrier to prevent migration of cations and penetration of moisture, (7) low-temperature (preferably <100°C for most of the semiconductors) and damage-free deposition, and (8) resilience to sputtering of subsequent layers. These requirements limit the materials choice and deposition techniques for the buffer layers (Figures 7A and 7B), as we summarized in the pros/cons of various deposition techniques in Figure 7C.

To compare deposition technologies' compatibility with buffer layers, we calculated figures of merit (FOMs) for each method. To do this, we first scaled each asset from 1 to 5 and visualized them in the spider chart (Figure 7C), where every two heptagons correspond to 1, and the last heptagon corresponds to 5 in scale. ALD is the slowest process among the deposition methods, and growing layers takes a long time; therefore, we considered it as 1, layers can be produced quickly in thermal evaporation (TE); we scored it as 5. In terms of low equipment cost, chemical bath deposition (CBD) is the cheapest one (1) such that one may need only a hot plate, magnetic stirrer, and container, whereas ALD (5) and chemical vapor deposition (CVD) (4) machines/apparatus are highly expensive. When it comes to processing complexity, spin-coating took the highest value (5) since pH, concentration, and temperature of solution and speed of rotation can significantly affect the nucleation and growth process and hence stoichiometry and quality of final layers, whereas CVD (1) and ALD (2) are vacuum-based methods, so controlling the growth process is relatively easy. According to these considerations, FOMs for each deposition method were calculated as follows:

$$\text{FOM}: \frac{\text{Sum of scaled positive factors}}{\text{Sum of scaled negative factors}} \quad \text{(Equation 1)}$$

in which positive factors are thickness control, conformality, deposition rate, low equipment cost, and low-temperature processability, while chemical damage and process complexity are negative ones. We found FOMs of CVD, CBD, TE, ALD, and spin-coating of the buffer layers as 3, 2.8, 2.5, 2.3, and 2.3, respectively. Even though the ALD and TE have extensively been employed to fabricate buffer layers, they demonstrated relatively low FOMs stemming from the equipment cost, which is an external factor that largely affects the calculation. The following subsections provide a more elaborate discussion on the previously reported buffer layers for solar cells and LEDs with various growth techniques with a cross-field learning perspective.

Solution-processing techniques

Solution-processing techniques are usually a primary choice for thin-film deposition due to their simplicity and low capital cost. Hence, not surprisingly, solution-processed buffer layers are frequently reported in the literature. For instance, presynthesized metal-oxide nanocrystals can be deposited as buffer layers via spin-casting, spray, or blade coating if the suspensions can be achieved in low-polarity solvents (since high-polarity solvents may damage underlying sensitive layers such as perovskite films or organic charge transport layers). Since these materials are presynthesized, preparing suspensions with low boiling point solvents (such as ethanol, isopropanol, etc.) allows for low-temperature processing (nevertheless, usually, a <100°C annealing step is needed to evaporate the solvent).[82] These advantages make this approach a suitable "soft" deposition technique for buffer-layer processing since the underlying sensitive layers can be kept undamaged. Here, the primary concern can be the chemical damage on the underlying layers with solvent interaction, which, as mentioned, can be mitigated by selecting an appropriate low-polarity solvent, if possible.

In the spin-casting technique, the thickness of buffer layers mainly relies on the rotation speed (in the case of spin casting) and the solution concentration. The uniformity and complete coverage (on flat substrates) can be ensured by controlling the size of nanoparticles and the surface roughness of the underlying layers. In this sense, ZnO (Figure 8A),[13,79,83] SnO_x (Figures 8B and 8C),[84] AZO,[11] ITO,[85] and WO_x[86] nanoparticles (average particle size is 15–100 nm, as exemplified with transmission electron microscopy images in Figure 8B) have been reported as buffer layers to protect the organic layers of PSCs, OSCs, and QLEDs. In addition, to protect against sputtering damage, SnO_2 nanoparticle-based thin films also exhibited good environmental stability under high humidity conditions when employed as a buffer layer in PSCs, as displayed in Figure 8C. In transparent QLEDs, ZnO nanoparticles and a blend of ZnMgO nanoparticles and polyvinylpyrrolidone have been utilized as a buffer layer.[87,88] Meanwhile, the library for metal-oxide nanoparticles is quite rich. For instance, Nb_2O_x, V_2O_x, NiO, and MgO nanoparticle-based thin films have been well documented for various applications.[89] Yet, these solution-processed nanoparticle thin films have yet to be utilized as buffer layers and deserve to be examined. Notably, the main disadvantage of spin-coating in this context (besides possible throughput and ineffective materials usage issues) is the incapability to deposit an ultrathin layer (<5 nm) since metal-oxide nanoparticles need a certain thickness to form a continuous film.[90] Solution-processed polyelectrolytes can also act as a buffer layer due to their high mechanical stability originating from long-chain structures. For instance, polyethyleneimine ethoxylated (PEIE) protects the sensitive C_{60} layer from sputter damage (Figures 8D and 8E). Its application to two-terminal (2T)

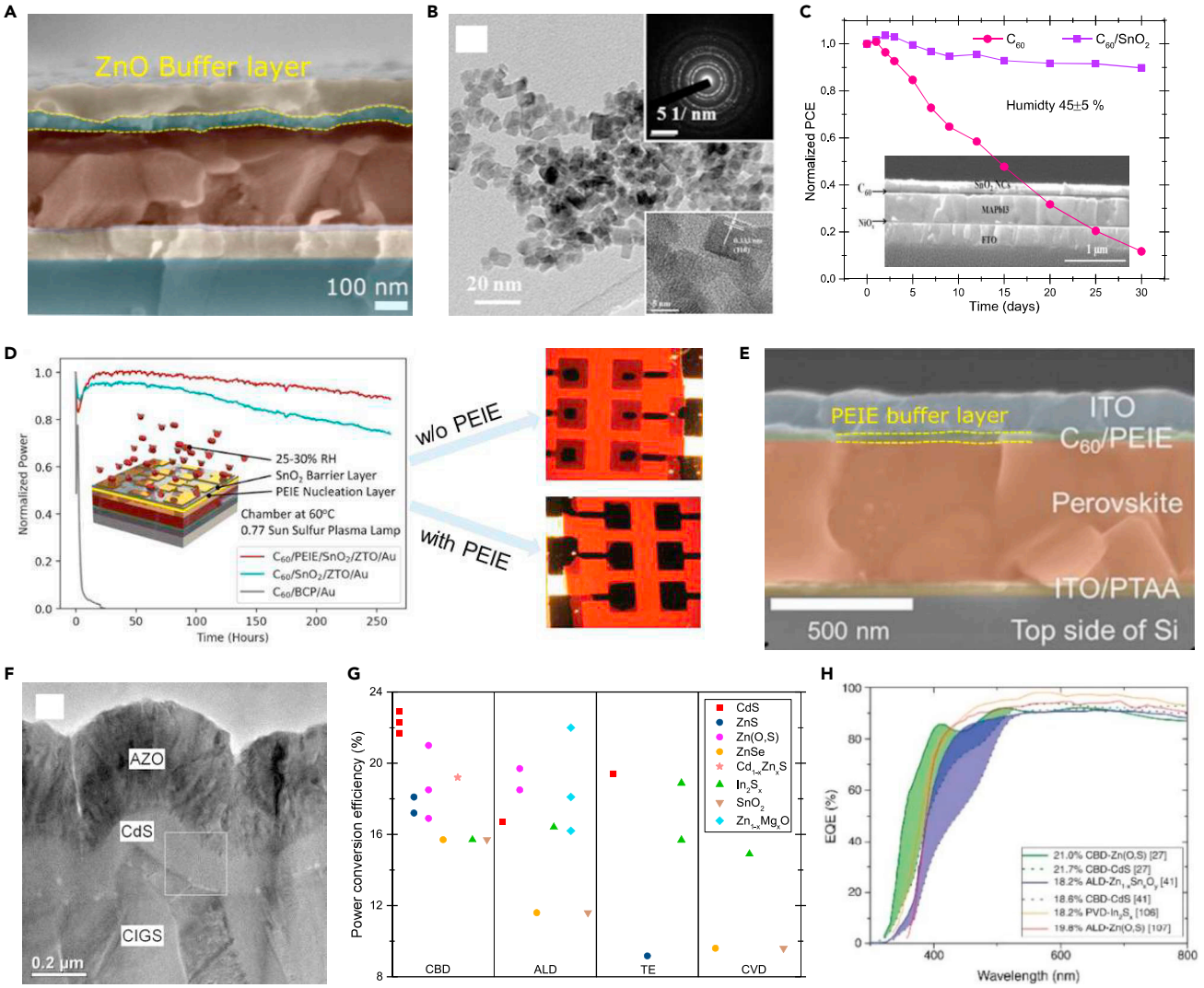

Figure 8. Solution-processed buffer layers for optoelectronic devices

(A) Cross-sectional SEM image of a *p-i-n* perovskite solar cell with solution-processed ZnO buffer layer. Reprinted with permission from Aydin et al.[13] Copyright 2019, Wiley-VCH.

(B) Bright-field transmission electron microscopy images of SnO_2 nanoparticle solution. Upper and bottom insets are corresponding diffraction patterns and high-resolution transmission electron microscopy images, respectively.

(C) Stability test of *p-i-n* PSCs with and without spin-coated SnO_2 buffer layer. The inset shows the SEM image of corresponding devices. Reprinted with permission from Zhu et al.[84] Copyright 2016, Wiley-VCH.

(D) Stability test results of unencapsulated PSCs with and without PEIE nucleation layers. Inset shows the device architecture and test conditions. Photographs of unencapsulated devices with and without PEIE layer after stability test done under N_2 environment and at 85°C over 670 h. Black regions show the remaining perovskite film after the stability test, and lighter regions on the metal pixels are correspond to areas where the Ag contact corroded due to halide diffusing. Reprinted with permission from Raiford et al.[94] Copyright 2019, Wiley-VCH.

(E) Cross-sectional SEM image of a *p-i-n* perovskite solar cell with solution-processed PEIE buffer layer between C_{60} and sputtered ITO. Reprinted with permission from Kim et al.[91] Copyright 2020, American Association for the Advancement of Science.

(F) Cross-sectional transmission electron microscopy image of sputtered AZO/chemical bath deposited CdS/CIGS structure. Reprinted with permission from Han et al.[95] Copyright 2014, Elsevier Inc.

(G) PCE values of CIGS devices with various buffer layers fabricated by different methods. Data are taken from Naghavi et al.,[96] Mughal et al.,[97] Gour et al.,[98] and Nakamura et al.[99]

(H) External quantum efficiency curves for CIGS cells with different buffer materials deposited by various methods. All cells include anti-reflection coatings, and shaded areas below the curves indicate the current gain relative to the corresponding CdS reference when available. Reprinted with permission from Feurer et al.[100] Copyright 2016, Wiley-VCH.

monolithic perovskite/silicon tandem solar cells resulted in a PCE of 26.7% with 76.4% certified *FF* (see Figure 8E for cross-sectional SEM image of the device).[91] These results show the equivalent performance of the PEIE layers as a buffer layer; however, how this layer prevents the sputter damage is still unclear, although electronically, it is known to act as a work function modifier of the TCOs.[92,93] Adapting the spin-casting technique to micron-scale rough surfaces, such as random pyramid textured crystalline silicon solar cells for tandem applications, is impractical (see Figure 7).[11,85] For such rough surfaces, spray coating can circumvent the limitations of the spin-coating technique and may therefore be suitable for scaling up the processing of such materials. However, no successful example has been reported for spray-coated buffer layers on large, textured substrates. Further research in this direction is required for definitive successful demonstrations on large, industrially applicable areas.

CBD, another solution-based technique, involves forming ionic species in a bath solution, followed by transport and condensation of these species on the substrate. The thickness, homogeneity, and density of the CBD-deposited films are linked with the choice of the solution (alkaline or acidic), composition and temperature of the solution, deposition time, and the substrate's surface properties.[101] In this case, cadmium sulfide (CdS)[102,103] (Figure 8F) and zinc sulfide (ZnS)[104,105] have been commonly used CBD-grown buffer layers enabling high and reproducible efficiencies of chalcopyrite and CdTe thin film solar cells. Meanwhile, the search for alternative CBD buffer layers is ongoing, with Zn(S, O), $Cd_{1-x}Zn_xO$, In_2S_3, and SnO_x as possible options. For CBD buffer-layer formation, the device stack is immersed into the bath and is subjected to advantageous chemical etching for removing oxides and other impurities of the device-exposed layer surface (for instance, CIGS or CdTe layer surfaces).[96] CBD-grown buffer layers established high-efficiency CIGS solar cells at low deposition temperature. However, this technique is not favorable on top of the perovskite and organic-based devices since the substrate is immersed primarily in an aqueous solution, likely leading to the dissolution of the underlying layers.[106] Also, the long waiting time (usually >10 min to hours) to reach the thickness of the required film is another drawback of the technique.[29]

Thermal evaporation

Surfaces that have rough features, such as random pyramidal textured silicon, 3D nanostructures, or large roughness depth to width ratio, usually require conformal coated buffer layers. Here, conformality signifies a film with a nearly constant thickness perpendicular to its underlying substrate surface. Nonconformal buffer layers typically do not provide sufficient protection in the thinner areas, whereas in thicker areas they may cause series resistance. Therefore, for such complex surfaces, vacuum-based thin-film deposition techniques are usually the first choice for several classes of materials. Its low particle energy (typically 0.3 eV or less)[107] and a high uniformity over a large area make TE a preferable "soft" technique for buffer-layer deposition for many optoelectronic devices.

Thermally evaporated metallic thin films, namely Ag,[108] Mg:Ag,[109] and bilayer of LiF/Al,[110] can be used as a buffer layer, as well as a semitransparent electrode, depending on the application. The initial development of top-emitting LEDs involved thin Mg:Ag layers on top of the emissive Alq_3 films.[111] While ~7.5-nm thin films were reported to be sufficient to prevent sputter damage, they led to elevated required operating voltages in the device. This was attributed to an almost complete oxidation of the Mg film during sputter deposition of ITO and incomplete coverage or

island-like formation of Mg:Ag films on the surface of the Alq_3 layer.[109] The use of relatively thicker (~10 nm) Mg:Ag buffer layers circumvented the problem mentioned above. However, the resultant top ITO electrode exhibited reduced transparency. The main drawback of evaporated metal buffer layers is forming island-like metal domains rather than continuous thin films, which might provide only limited protection from subsequent sputtering. Moreover, evaporated metal buffer layers have low optical transparency.[112] One of the strategies to improve film coverage is surface treatments or use of adhesion layers, e.g., depositing an ultrathin (1 nm) layer of Cr between the HTL and Au electrode.[113]

One can expect that SnO_x, ZnO, NiO_x, and CuO_x, as *n*- and *p*-type oxides, respectively, can be good candidates as thermally evaporated buffer layers. However, usually, these materials do not melt or sublime effectively, resulting in flawed films. E-beam evaporation is a more effective fabrication method for such materials, but the resulting X-ray radiation produced by the EB (also referred to as *bremsstrahlung*) might damage the substrate.[114] So far, transition metal oxides, such as MoO_x, V_2O_x, and WO_x, are the most successful examples of thermally evaporated buffer layers.[12,115–119] Their high work function values give them the character of *p*-type, electron-blocking materials in solar cells and LEDs.[118,120,121] For fabricating top-emitting or transparent OLEDs, moderately thick metal oxides such as MoO_x[122] and WO_x[123] are frequently incorporated as buffer layers due to their relatively high transparency, the visible region, and their simple thermal evaporation-based deposition. Similarly, the insertion of evaporated MoO_x and V_2O_x buffer layers between the photoactive QD layer and metal electrode in opaque QDSCs enables environmental protection by blocking oxygen and water diffusion and reduces the Schottky barrier height at the contact interface. This leads to enhanced hole extraction, resulting in improved device performances.[124,125]

From an optical perspective, the moderate bandgap of V_2O_x (2.1 eV), which leads to strong parasitic absorption in the blue part of the solar spectrum, makes it less attractive for application at the sun-facing side in solar cell applications when compared with MoO_x (3.1 eV) and WO_x (3.3 eV) (Figure 9A).[126] Also, oxygen vacancies generate positively charged structural defect states that act as localized color centers, leading to absorption in the visible (VIS, 400–700 nm) and near-infrared (NIR, 700–1100 nm) parts of the spectrum, depending on their oxidation states.[126] Notably, the widely used MoO_x buffer layer can suffer from the same issue.[127] Using such buffer layers requires careful thickness optimization to achieve continuous films, which may come with the cost of increased parasitic absorption. For instance, optimal performance of OLEDs with WO_x have been achieved with 60-nm-thick films (Figure 9B); thinner films suffered from low surface coverage, whereas thicker films led to increased parasitic absorption.[123]

From a stability perspective, MoO_x can be a source of degradation in devices. For instance, the iodine released from the perovskite layer can react with MoO_x, leading to iodine-deficient surfaces.[131] Considering the higher standard reduction potential of WO_3 (−0.09 E^o/V) than MoO_3 (+0.075 E^o/V) makes WO_3 a better candidate in terms of stability.[126] In addition, MgO_x (>4.5 eV) and CrO_x (~3.4 eV) feature high bandgap values and can be thermally evaporated, which make them suitable future candidates to replace MoO_x buffer layers underneath sputtered TCOs.[132,133] Nevertheless, inserting a thin layer of wide bandgap conjugated molecules with free lone pairs such as 2,2′,2″-(1,3,5-benzinetriyl)-tris(1-phenyl-1-H-benzimidazole) (TPBi) or bathocuproine (BCP) between MoO_3 and the HTL (Figure 9C) can prevent the

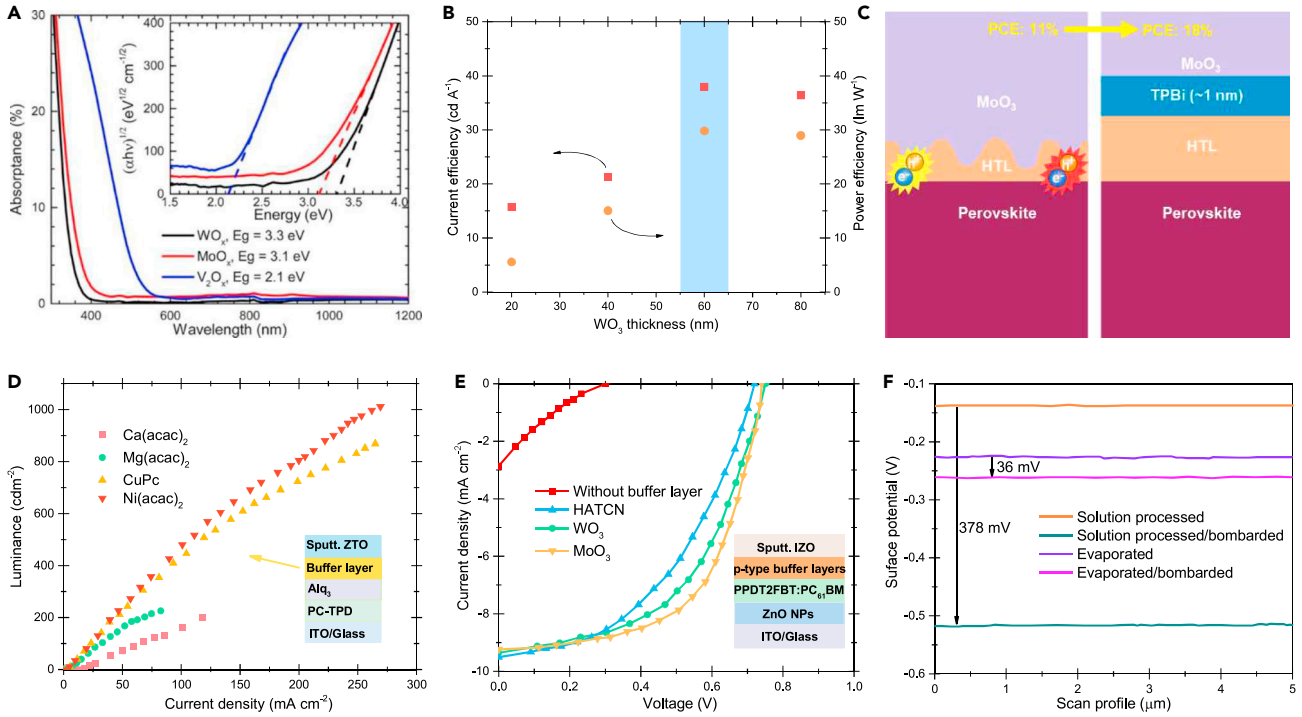

Figure 9. Thermally evaporated buffer layers in optoelectronic devices

(A) Absorptance spectra of widely used hole-selective inorganic buffer layers (in ~10-nm-thick evaporated MoO_x, WO_x, and VO_x layers on glass). The inset is Tauc plots of corresponding buffer layers depicting their bandgaps. Reprinted with permission from Werner et al.[126] Copyright 2016, American Chemical Society.

(B) Current and power efficiency of transparent OLEDs with respect to varying thickness of WO_3 buffer layer plotted at 100 cdm^{-2}. The aqua area around 60 nm WO_3 indicates the optimum buffer-layer thickness. Reprinted with permission from Meyer et al.[123] Copyright 2008, Wiley-VCH.

(C) The schematic illustrates influence of the insertion of TPBi organic film between HTL (spiro-OMeTAD) and evaporated MoO_3 buffer layer in PSCs. Adapted from Perez-del-Rey et al.[128]

(D) Luminance–current density characteristics of transparent OLED devices with evaporated metal acetate buffer layers. The inset depicts device structure employed for measurements. Adapted from Yamamori et al.[129]

(E) Current density-voltage curves of semitransparent OSCs using various p-type buffer layers. The inset shows device structure used for measurements. Adapted from Kuwano et al.[86]

(F) The variation in surface potential profiles of solution-processed BCP (on PCBM) and evaporated BCP (on C_{60}) buffer layer before and after IZO bombardment. Adapted from Ying et al.[130]

diffusion of MoO_x into the underlying layer and can extend the stability and performance of PSCs.[128]

Thermally evaporated organic materials like copper phthalocyanine (CuPc), zinc phthalocyanine (ZnPc),[134,135] metal acetylacetonate complexes,[129] pentacene,[136] and 1,4,5,8,9,11-hexaazatriphenylenehexacarbonitrile (HATCN)[137] can function as buffer layers if the TCO deposition power density is low enough. Figure 10 shows the chemical structures of such commonly used organic buffer layers. The sputter damage on the robust and chemically inert organic molecules such CuPc and 3,4,9,10-perylene tetracarboxylic dianhydride (PTCDA) is limited. This resilience is usually attributed to the dissipation of collision energies among several neighboring lattice molecules.[134] Moreover, the electron injection from ITO to the lowest unoccupied molecular orbital of the organic semiconductor was reported to occur via a high density of sputter-induced mid-gap defect states in the buffer layers. Since CuPc absorbs light in the visible range, an alternative layer of BCP was also incorporated as a buffer layer for top illuminated or emitting devices. Figure 10B summarizes the normalized absorbance spectrum of common organic buffer layers.[138] The

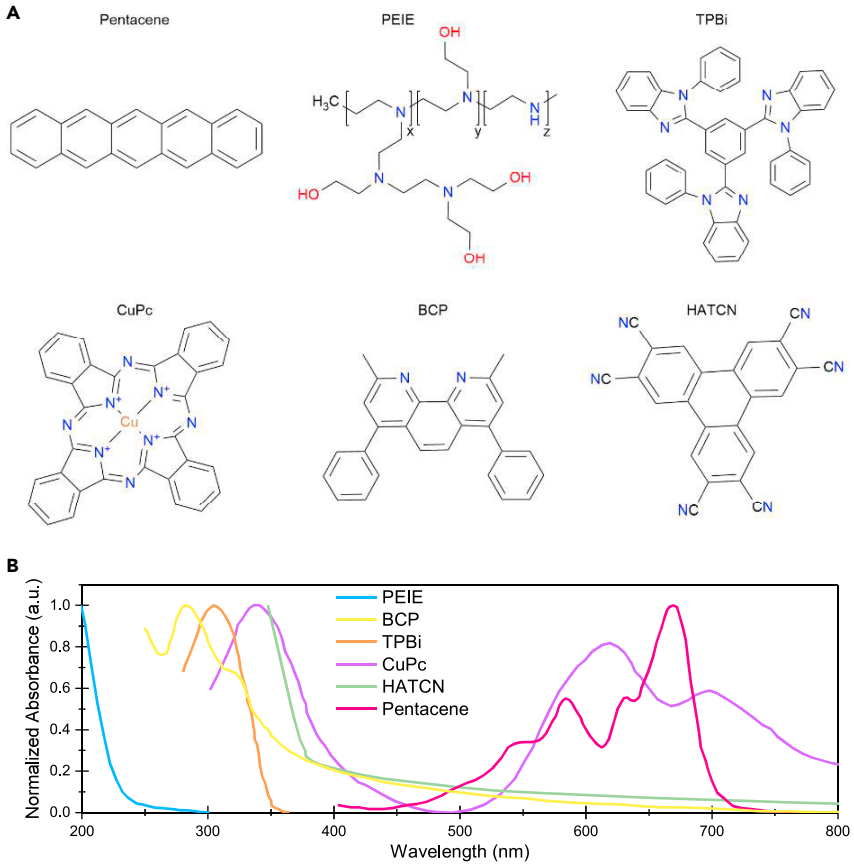

Figure 10. Organic compounds commonly used as buffer layers in optoelectronic devices
(A) Chemical structures of various organic buffer layers used in solar cells and LEDs.
(B) Normalized absorbance spectrum of various thin films used as organic buffer layers (PEIE/quartz,[139] BCP/ITO/glass,[140] TPBi/fused silica,[141] CuPc/glass,[142] HATCN/quartz,[143] Pentacene/glass[144]).

replacement of CuPc with the BCP buffer layer was particularly beneficial for red-emitting OLEDs. We note that in both CuPc and BCP buffer layers, ITO was sputter-deposited at a relatively low rate of 0.3 Å/s, respectively.

Further, the injection efficiencies in both the devices were shown to improve upon deposition of a ~3 Å and ~ 5 to 10 Å Li layer between the CuPc and ITO and the BCP and ITO, respectively.[145,146] As an alternative, an equivalently thick (43 nm) pentacene film has been reported as a buffer layer for protection against sputter damage; however, this resulted in a lower device efficiency due to the strong parasitic absorption of light in pentacene.[136] Also, the surface morphology of planar molecules, e.g., pentacene, forms polycrystalline films, which affect the growth of ITO on top of it and consequently limit the conductivity and transparency of the overlying ITO. To overcome this limitation, a thin layer of spin-coated PEDOT:PSS onto pentacene can reduce the surface roughness and provide better ITO growth.[147] Although transparent OLEDs containing CuPc or pentacene buffer layers achieved up to 80% optical transparency, both materials exhibit substantial absorption losses in the VIS spectrum. Therefore, another buffer layer, such as nickel acetylacetonate, offers negligible absorption in the VIS range with good electron injection properties analogous to the CuPc buffer layer, resulting in better device performances in

OLEDs (Figure 9D).[129] HATCN is also reported to be a buffer layer with an impressive hole injection property and chemical stability against oxygen.[137] Owing to its high transparency in the visible spectrum and a low refractive index of ~1.7, the HATCN buffer layer has been extensively used in inverted OLED devices.[137,148–150] In addition, its planar discoid shape allows it to be stacked densely on the substrate when thermally evaporated. Taking this advantage, OSCs with an HATCN buffer layer exhibited promising device performance on par with their metal-oxide counterparts, as shown in Figure 9E.[86] These organic molecules carry a high potential to be applied as a buffer layer in PSCs and OSCs, which is an opportunity yet to explore.

Further, vacuum-evaporated materials may show better tolerance to particle bombardment in the TCO sputtering process than their solution-processed counterparts.[130] For instance, comparing the spin-coated and thermally evaporated C_{60}, the surface potential of the C_{60} layer shifts ~36 mV for evaporated ones and ~378 mV for the solution-processed counterparts, according to Kelvin probe force microscopy measurements (Figure 9F). The substantial increase in defect densities at the interfaces of solution-processed layers due to the bombardment (as indicated by the shift of surface potential) accounts for significant variations in reported device performances.[130] Still, one of the disadvantages of thermally evaporated buffer layers is their rougher surface morphology and requirement of specific thickness values (in general >10 nm) to have continuous and pin-hole-free films, which is needed for adequate protection against sputter damage. Therefore, several previous studies focused on the critical role of film thickness.[151,152] The common observation from these experiments is insufficient protection if the film is too thin or an increase in series resistance if the film is too thick. To conclude, TE offers solvent-free and physical deposition of buffer layers without involving high energetic particles. This simplicity makes the technique suitable for buffer-layer deposition, but achieving continuous ultrathin films with high optical transparency is still open to further investigation.

Chemical vapor deposition techniques

For conformal and pinhole-free buffer layers on complex surfaces, CVD-based techniques offer unique advantages. For instance, ALD, the most widely used technique for buffer layers among all CVD techniques, involves thin-film formation based on sequential, self-limiting chemical reactions of the precursors. During film growth, the adsorption of precursor on the substrate is a nondirectional process driven by diffusion, creating excellent coverage on all surfaces, a desirable property to form a continuous film.[153] In contrast, if self-limiting behavior cannot be achieved, the overall process is termed pulsed CVD.[154] The combination of low-temperature processability and sub-nanometer thickness control makes ALD an ideal "soft" deposition technique for buffer layers (Figure 7).[155] More importantly, ALD is adaptable for mass production since it allows the deposition of multiple substrates in cassettes in a single batch. The precursor choice must be a critical step to let the film grow at low temperatures, and this precursor should not be reacting with the underlying layers. Also, processes usually require hydroxyl (−OH) groups on the underlying layer to initiate film growth. Therefore, sometimes different surface treatments, such as UV-ozone exposure (if applicable without damage)[156] or utilization of ultrathin nucleation layers might be needed.[157] For instance, inserting –OH-rich PEIE layers as a base layer for ALD films results in denser films on soft layers and brings additional advantages in terms of chemical resistance of such coatings.[94] Currently, the main drawback of conventional ALD is its relatively slow deposition rate and the high capital investment of the equipment. For mass production, spatial ALD can provide a higher deposition rate

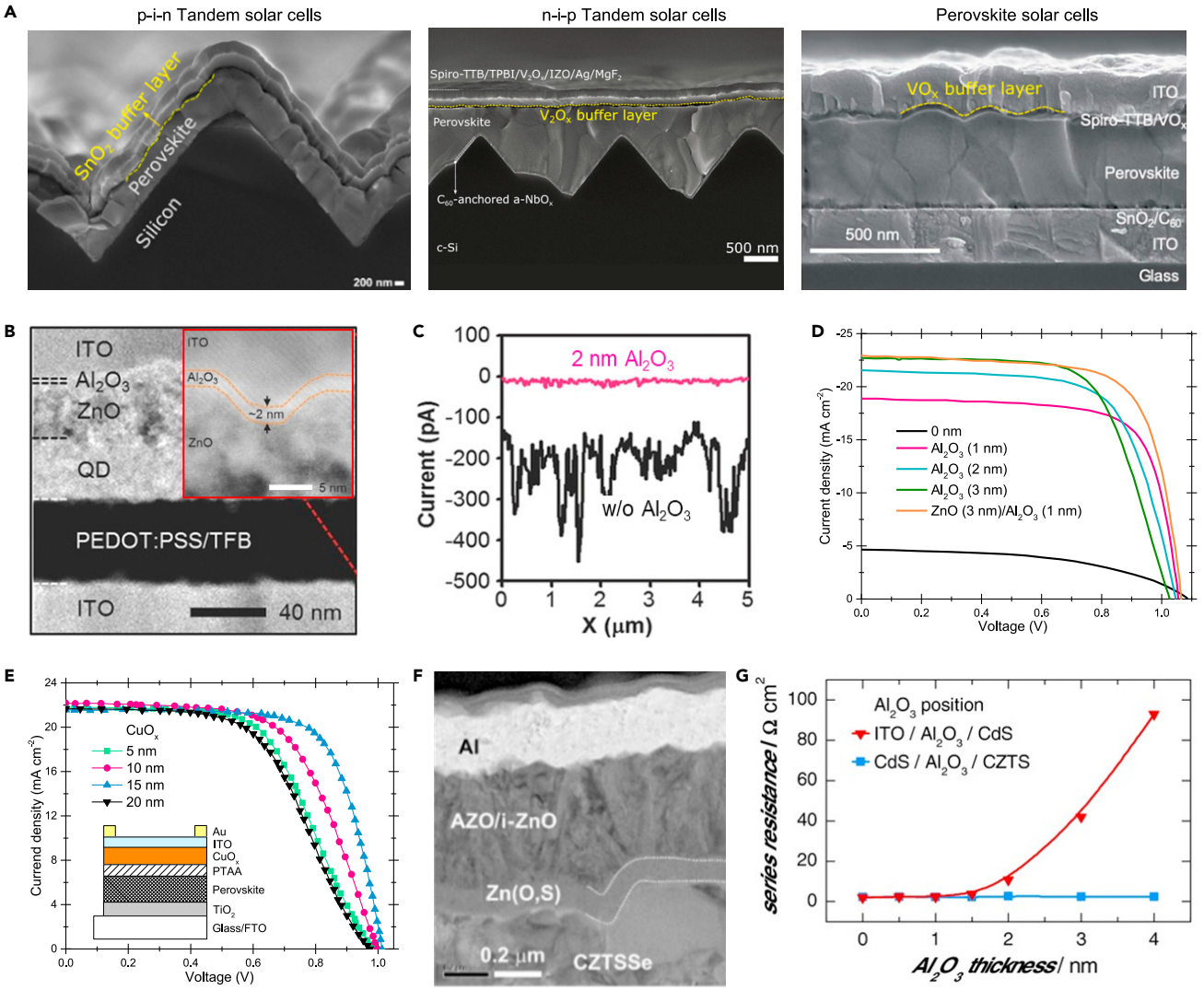

Figure 11. Chemical vapor deposited buffer layers in optoelectronic devices

(A) Cross-sectional SEM images of ALD SnO_2 and VO_x buffer layers used in various single-junction and tandem solar cells. SnO_2 image was reprinted with permission from Aydin et al.[52] Copyright 2020, Springer Nature. V_2O_x image of tandem configuration was reprinted from Aydin et al.[163] V_2O_x image of single-junction perovskite solar cell was reprinted with permission from Raiofer et al.[161] Copyright 2019, The Royal Society of Chemistry.

(B) Transmission electron microscopy images of transparent QLEDs with ALD deposited Al_2O_3 buffer layer and sputtered ITO films. The inset in the red square shows the magnified image of a sputtered ITO/ALD Al_2O_3/ZnO section (Note: The scale bar in the inset represents 5 nm).

(C) Current distribution of ITO/HTL/QDs/ZnO/Al_2O_3 structures (shown in B) characterized by conductive atomic force microscopy. Reprinted with permission from Choi et al.[80] Copyright 2017, Wiley-VCH.

(D) Current-voltage characteristics of semitransparent PSCs with ALD Al_2O_3 buffer layer in different thicknesses and ALD Al_2O_3/ZnO bilayer. Adapted from Rajbhandari et al.[162]

(E) Current density versus voltage curves of semitransparent perovskite devices with varying buffer thickness of CuO_x. Inset shows the device structure used for measurements. Adapted from Eom et al.[164]

(F) Cross-sectional transmission electron microscopy images of CZTSSe solar cells with atomic layer deposited Zn(O, S) buffer layer. Reprinted with permission from Hong et al.[165] Copyright 2016, Elsevier Inc.

(G) Series resistance values of CZTSSe devices were plotted as a function of ALD Al_2O_3 layer thickness for both passivation (on CZTSSe) and buffer layer (on CdS). Reprinted with permission from Lee et al.[67] Copyright 2016, Wiley-VCH.

thanks to separating the precursors in space rather than in time. For spatial ALD, highly volatile precursors are needed, which may limit the choice of buffer-layer materials. Pulsed ALD can accelerate the process, but it should be noted that pulses might damage the soft layers.[158]

Thanks to the advantages mentioned above, ALD metal oxides have found several applications in optoelectronic devices. For instance, SnO_x and ZnO-based buffer layers are frequently utilized in PSCs and perovskite/silicon tandem solar cells if the light is incident on the *n*-type contact side,[53,55,159,160] whereas VO_x is used if the light is incident from the *p*-type contact side (see examples for solar cells in Figures 11A).[161] Although diverse *n*-type metal-oxide materials are available (such as TiO_x, Nb_2O_x, and In_2O_x), SnO_x is still dominant due to its broadband transparency, relatively high carrier concentration, therefore, high conductivity, and high chemical stability.[58] Alternatively, ultrathin Al_2O_3 also can be used as a buffer layer. Al_2O_3 is a highly insulating material, but after carefully reducing its thickness, it can function as a buffer layer, as reported in QLEDs and PSCs (Figures 11B–11D).[80,162] An ALD Al_2O_x layer as thin as 2 nm inserted between the charge transport layer and sputtered ITO in QLEDs was reported (Figures 11B), preventing plasma damage and thus enabling remarkably enhanced device operational lifetimes (from less than 1 h to over 23 h).[80] In addition, such ALD Al_2O_x buffer layers significantly improved the areal homogeneity of the current distribution and prevented short-circuiting the devices (Figure 11C), resulting in total luminance (sum of bottom and top emission) of 73,000 cd m^{-2} at 9V, which was among the highest at that time. Similarly, ALD Al_2O_x buffer layers have been utilized to improve device performances of PSCs, as shown in Figure 11D.[162]

In general, the optoelectronic properties of ALD buffer layers can be tuned to some extent by processing temperature and pulse-purge conditions in the ALD.[166] Among the transition metal oxides, V_2O_x seems an ideal material since only V_2O_x appears to have a precursor solution that allows for deposition at a temperature below 100°C.[161,167,168] Low processing temperatures are critical for "sensitive" layers such as metal-halide perovskites due to their degradation at higher temperatures (>80°C, usually by the release of organic cations, e.g., MA^+).[169] The successful application of ALD V_2O_x buffer layers has been demonstrated for *n-i-p* perovskite/silicon tandem and single-junction solar cells (see Figure 11A).[161,163]

Furthermore, ALD allows for achieving more complex buffer-layer materials, such as ternary ZnSnO (ZTO), which has been successfully demonstrated in PSCs.[170] An ultrathin bilayer of SnO_x and ZTO exhibits better buffer-layer behavior in which the SnO_x prevents the penetration of zinc into the perovskite layer, while the ZTO provides a low-contact resistance with ITO.[50,170] The benefits of the ALD buffer layer become more vital, especially for all-perovskite and perovskite/organic tandem solar cells, where the recombination junction must be deposited on top of a high bandgap absorber to interconnect the sub-cells electrically.[171,172] For instance, the ALD bilayer of SnO_x-ZTO can protect the sputtering process of the ITO recombination junction layer.[173] Moreover, ALD encapsulation layers (ZrO_x and Al_2O_x) are widely employed in OLEDs,[174] and were recently demonstrated to be feasible in PSCs using low-temperature processes.[175] Despite its successful application in solar cells, using an ALD buffer layer in inverted OLEDs, OSCs, and QDSCs has not been explored yet and is worth further investigation.

Atmospheric pressure CVD (AP-CVD) is an excellent alternative to conventional ALD for fast and cost-efficient processing.[164] Although ALD and AP-CVD use similar precursors, the AP-CVD technique mixes precursors in the gas phase to obtain CVD rather than self-limiting growth, which accelerates the growth of the film. For a simple comparison, 15 nm of CuO_x can be acquired by pulsed CVD within 24 min, whereas it would take 4 h by conventional ALD to obtain the same material.[164] Like ALD, this method forms thin films by the reaction of precursors either in the gas phase or on the substrate's surface, but AP-CVD does not require a high vacuum. Despite these advantages, few studies have been demonstrated to fabricate buffer

layers via AP-CVD. For *p*-type materials, successful plasma-damage protection by CuO_x buffer layers of *n-i-p* PSCs has been reported (Figure 11E).[164] This can be an excellent alternative to ALD V_2O_x and thermally evaporated MoO_x buffer layers, owing to the high transparency in the infrared region of CuO_x and its high thermal stability under operation. Moreover, its processability at 100°C with the CVD method makes it suitable for several temperature-sensitive optoelectronic devices.[38] For *n*-type materials, ZnO, TiO_x, and SnO_x, have been implemented with the AP-CVD method.[176] It should be noted that the growth rate usually follows an inverse trend with the temperature, and high temperatures might be harmful to the devices. For instance, processing above 110°C is reported as harmful for perovskite layers since the organic cation leaves from the surface at high temperatures.[158] Hence, the deposition rate (and therefore processing temperature) should be set considering the temperature sensitivity of the soft layers.

In thin-film CZTSSe and CIGS solar cells, ALD is widely used to enable conformal coating of buffer layers on rough surfaces of absorber layers (Figure 11F). CIGS devices with CBD Zn(O, S)/ALD $Zn_xMg_{1-x}O$ double-buffer layers hold the current record PCE of 23.5%.[99,165,177] In addition, insertion of a thin layer of ALD Al_2O_x (0.5 nm) between CdS and ITO may protect CdS against sputtering damage and thus reduce V_{OC} deficit in CZTSSe devices; however, careful tuning of Al_2O_x thickness is needed to avoid a severe increase in series resistances, as depicted in Figure 11G.[67]

STRATEGIES FOR TRANSPARENT ELECTRODE DEPOSITION TO ELIMINATE BUFFER-LAYER USAGE

Sputtering process optimization and new sputtering hardware design

Rather than using an additional buffer layer, adding processing costs, several approaches have been discussed to minimize the sputtering damage on sensitive layers. These efforts include lowering the power density,[178] changing the sputter gas or gas pressure,[76,179] using facing-target sputtering (FTS),[180] and combining low- and high-power sputtering in a two-step process.[123,181]

For magnetron sputtering (as sketched in Figure 12A), there is no consensus on which power density value can result in a damage-free deposition. For instance, the power density of 0.07 W cm^{-2} (40 W with a 507 cm^2 ITO target) has been reported as not causing damage to spiro-OMeTAD in PSCs.[178] On the other hand, an RF power density of 0.4 W cm^{-2} enabled the deposition of ITO directly on PTAA without causing damage, which may be a good benchmark for further development.[178] Generally, the power density for sputtered TCOs used in PSCs varies from 0.76 W cm^{-2} to 4.4 W cm^{-2}.[12,38] Target-to-substrate distance, sputtering gas, and process pressure are essential parameters among others to consider to reduce the power density threshold. Regarding the effect of background gas during sputtering, a replacement of Ar with Kr has been shown to reduce the kinetic energy of sputtered atoms, as revealed in a more significant photoluminescence intensity BAlq deposited in Kr than those deposited in Ar gas.[179] Besides the gas composition, an increase in the total gas pressure can lower the kinetic energy of atomic particles by minimizing the energy of sputtered particles.[179] Another approach to overcome the heating issue on the sensitive films is intermittent sputtering deposition sequence. For instance, opening the shutter for 1 s every 7 s during the deposition enables direct sputtering on metal acetylacetonate complexes without thermal damage.[129]

Additionally, post-annealing the device stack after sputtering at mild temperatures (such as ~90–100°C) might help mitigate the *S*-shape *I-V* curve behavior. The short

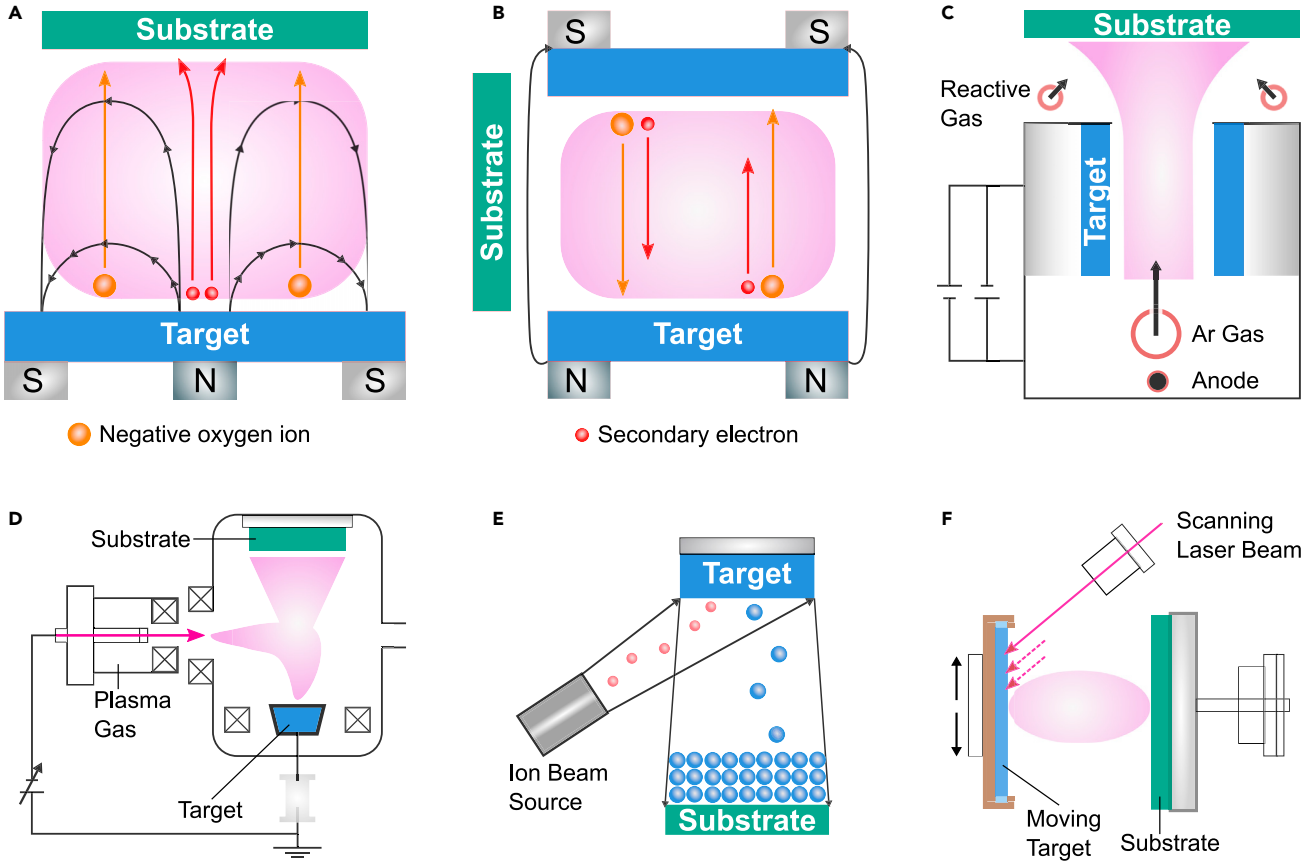

Figure 12. Schematic demonstrations of alternative advanced sputtering designs and other alternative PVD techniques for "soft-landing" deposition

(A) Magnetron sputtering.

(B) Facing target sputtering.

(C) Gas-flow sputtering system.

(D) Reactive plasma deposition (hollow cathode ion plating).

(E) Ion beam sputtering.

(F) Pulsed laser deposition.

annealing step can passivate the shallow trap states deeper in the perovskite layer by the diffusion of PCBM into the grain boundaries of the perovskite film. A similar approach of post-annealing after direct growth of ITO (sputtering at 1.1 W cm^{-2} power density) onto spiro-OMeTAD achieved the most efficient buffer-layer-free semi-transparent PSCs (PCE of 15.7%) at that time.[182]

Although several successful attempts of direct TCO sputtering on top of transport layers have been demonstrated, most studies on sputtering damage in optoelectronic devices have been primarily focused on linking the external process parameters to the device performance. However, establishing these correlations to the plasma parameters such as the ion energy may serve as a basis for a more systematic approach toward the TCO deposition optimization. As discussed in the section "origins of damage during magnetron sputtering of TCOs," negative ions are the most energetic species and are strong candidates to be the primary source of degradation. Therefore, one crucial milestone to enable damage-free deposition of transparent electrodes with the desired optoelectronic properties and acceptable deposition rates using the current magnetron sputtering processes lies in mitigating the bombardment by negative ions. There are

two possible strategies to follow: (1) lowering the target voltage during the sputtering and (2) physically separating the target from the substrate.

Enhancing the plasma density can be partially achieved by tuning the processing parameters. For instance, monitoring the target voltage may give insights into reducing the maximum kinetic energy of the negative oxygen ions. It was previously shown that lowering the power density[40] and increasing the process pressure[183] leads to the decreased discharge voltage, which agrees with the reported observations from the device reports as discussed above. However, the preferred and more efficient way to lower the target voltage without compromising the deposition rate and sputtering yield would be to increase the ionization of the plasma without additional negative ions acceleration. These may require upgrading the existing hardware, such as follows:

1. RF plasma excitation.[184] Preferably, switching to higher RF frequencies such as 27.12 MHz.[185]
2. Use of rotatable magnetrons[62] (and/or stronger magnets[40] for existing sputtering systems).

Another approach lies in placing substrates, not in direct sight of the target. This also implies modified designs of the currently used magnetron sputtering equipment to the following configurations:

1. FTS[186]
2. Gas-flow sputtering (GFS)[187] or hollow cathode sputtering
3. Off-axis sputtering[188,189]

For instance, FTS has no direct irradiation of a high-density plasma on the device (unlike conventional sputtering), offering possibilities to reduce damage during TCO deposition.[77] A magnet is applied behind two targets that form a homogeneous magnetic field to limit the charged energetic particles (see the sketch in Figure 12B). Thus, the charged electrons and ions move perpendicularly between the targets. The substrate, placed out of the plasma region, is not directly affected by the strike of high energetic particles.[180,190] The average energy of atoms bombarding the substrate in FTS is around 0.2 to 0.5 eV due to the short mean free path in the plasma region, which is much lower than conventional sputtering.[39,42] As severe bombardment is absent during FTS, neither thermally induced degradation nor defects occur to the organic layer.[45,181,191]

The two-step linear FTS process of InZnSnO (IZTO) top electrode for semitransparent PSCs is an excellent example of this.[181] A slow sputtering (low damage) process followed by a fast sputtering method in the second step results in a higher deposition rate of FTS (44 nm min $^{-1}$) than conventional sputtering of ITO (20 nm min^{-1}). Moreover, two-step RF sputtering (50 W/150 W) of an IZO top electrode applied to transparent QLEDs, led to performances better than standard one-step sputtering of IZO (150 W) and on par with nondestructive evaporated Al counterparts.[192] Similarly, this technique is used for ITO top electrode deposition in OLEDs to prevent severe sputtering damage.[123,193,194] The suppression of damage in FTS can be further improved by inserting the shield plates near the targets and generating a magnetic field from magnets near the substrate holder.[190] This modification effectively restrains the incidence of the secondary electrons on the substrate when the top ITO layer is deposited in an OLED device.[180,190]

As mentioned previously, hollow cathode glow discharge, resulting in high plasma densities, may be advantageous for "soft-landing" deposition. For instance, in GFS, ejected particles are thermalized and carried toward the substrate by an intense gas flow (Figure 12C). GFS was shown to cause a smaller decrease in c-Si passivation quality than DC sputtering as relevant for application in SHJ cells.[45] This may also be attributed, in part, to the high working pressure during GFS (typically in the mbar range).

Another hollow cathode-based method is reactive plasma deposition (also known as hollow cathode discharge ion plating), shown in Figure 12D. In contrast to the magnetron sputtering, it operates in arc mode rather than a glow discharge, ensuring lower working voltages. Furthermore, reactive plasma deposition (Figure 12D) has been successfully utilized to fabricate ZnO-based and W-doped In_2O_3 transparent electrodes for CIGS and SHJ applications.[195,196]

In summary, combining a softer sputtering technique, a two-step process, and/or a mild thermal posttreatment could be the cornerstone of depositing an electrode onto perovskite, organic layers, or QDs.

Alternative "soft-landing" techniques for transparent conductive oxide deposition

While the sputtering damage can be reduced by modifying the deposition processes, alternative soft-landing deposition methods can eliminate the buffer-layer usage. Ion beam sputtering (IBS) and PLD have also been investigated among PVD methods for damage-free TCO deposition for optoelectronic devices. High-performing ITO deposited by IBS (see the sketch in Figure 12E) on PET substrates at low temperatures (<150°C) was implemented in flexible OLEDs as the front electrode.[197] Unfortunately, there are very limited studies on IBS deposition on top of functional layers. Previously, damage-free deposition of Al by IBS for blue bottom-emitting OLEDs was demonstrated.[198] The impact of high-energy particles is partially mitigated thanks to the tool's geometry, where the substrate is only exposed to the secondary electrons from the target. In contrast, the plasma is only contained in the ion source. In the same work, magnetic traps were successfully implemented to significantly reduce charge particle impingement as measured by a cylindrical energy analyzer.[198] On the other hand, an indium oxide (In_2O_3) capping layer was deposited on top of transparent OLEDs via modified two-step IBS method, in which argon and oxygen ion sputtering were sequentially employed to obtain bilayer 5 nm/95 nm In_2O_3 films, where the role of the first layer is to reduce damage to, and prevent oxidation of, underlying layers.[199]

PLD, in its turn (Figure 12F), has an advantage of the near-stoichiometric transfer of target compounds and has also been demonstrated as an alternative technique for damage-free deposition in solar cells and LEDs. Room temperature PLD-deposited IZRO applied as a rear electrode in buffer-free semitransparent PSCs enabled higher efficiencies (15.1%) than those with sputtered ITO (11.9%).[200] The standard PLD of TCOs as top electrodes for OSCs was reported to still lead to substantial impact damage to the organic layers by high-energy particles during deposition.[201] Alternatively, eclipse PLD (whereby a circular shadow mask with a diameter of 19.4 mm is installed between the target and the sample) in an Ar atmosphere to prepare the top electrode of OSCs could enable devices with efficiencies similar to the reference device, which employed a thin metal electrode. Moreover, AZO-based TCOs fabricated by PLD were implemented on CIGS solar cells and OLEDs as transparent top electrodes; however, both devices utilized buffer layers (CdS/ZnO for CIGS cells,

WO_x for OLEDs) to mitigate process damage.[202,203] Current experimental evidence suggests that the success in developing damage-free deposition by PLD lies in reducing the energy of the arriving species through thermalization via the background gas at elevated deposition pressures (compared with sputtering). This is enabled by a more extensive choice of process pressure, as the source of the material ablation (excimer laser) is physically decoupled from the vacuum chamber. However, other potential effects such as possibly intrinsically different ion energy distributions during laser ablation or smaller plasma imprint on the substrates due to the highly confined PLD plasma are much less studied and cannot be entirely discarded.

As mentioned in the previous section, CVD-based techniques, mainly ALD, are attractive candidates for the buffer layers and damage-free deposition of the transparent electrodes themselves. So far, high-quality AZO, IZO, and ITO layers have been prepared by ALD on glass substrates.[204,205] Studies have shown that the desired materials can be deposited at a range of temperatures known as "ALD temperature windows" depending on the precursors used. The deposition within the ALD temperature window is needed to obtain the desired material properties comparable to those deposited via conventional sputtering. For example, ALD deposited AZO top electrodes were successfully implemented on OLEDs.[202] As discussed above, the optimum processing temperature of AZO at 150°C is a challenging ALD application for thermally vulnerable materials such as organic or perovskite compounds, which implies that alternative precursors should be studied. Also, plasma-enhanced ALD (PE-ALD) can obtain high-quality materials at lower temperatures, but one must consider how this process might affect the device. Reports on PE-ALD for top electrodes are limited so far and warrant further work.[206] Also, conventional ALD is usually considered a slower deposition technique than sputtering, specifically for thick films. Spatial ALD, in which the precursors are separated in space rather than in time, may accelerate the processing speed for TEs. On the other hand, B-doped ZnO layers have been implemented by metal-organic CVD (MOCVD) to SHJs as an alternative TCO to sputtered ITO, exhibiting good optical properties while having some electrical drawbacks due to aging of the layers, which can be solved by further studies and might be a promising technique to replace sputtering.[207]

CONCLUSION AND OUTLOOK

Beyond the state-of-the-art, buffer-layer/TCO stacks hold great promise for applications where high transparency and (semi)conductivity are needed, not only for LEDs and PVs, but also a wide range of applications such as semitransparent conductors, field-effect transistors, thermal shields, and photo-detectors, to name a few. However, the frequently used magnetron sputtering method for the transparent electrodes causes inevitable damage to soft layers such as perovskites and organic films. The insertion of an underlying buffer layer is still the most preferred solution to limit or mitigate the effects of sputter damage, and while there is no universal buffer-layer material and no preferred deposition technique, our review provides cross-field learnings to explore different materials for the specific device application.

We argue that optimization of the sputtering process, as the most established mean of fabricating transparent electrodes, has not yet been fully explored. Linking plasma properties to the interface degradation may be the pathway to deeper understanding and associated device improvements, potentially eliminating the requirement for the buffer layer. In general, effort should be focused on mitigating

the highly energized particles during sputtering. This can be achieved by increasing the plasma ionization and/or changing the tool geometry to minimize the plasma imprint on the substrate, such as FTS or GFS.

For the development of alternative TCOs, the previously counted key criteria need to be satisfied, regardless of the deposition technique. Several emerging techniques, such as PLD, IBS, or ALD, fulfill some of these criteria. However, sufficient throughput should be verified to employ the full potential of these techniques in mass production. ALD seems to be the most advanced technology that allows low-temperature deposition and produces conformal thin films. In this case, research effort should be put into finding alternative precursors to allow for low deposition temperatures. In addition, the use of remote plasma ALD might be worth investigating. In the future, more work needs to be done to make these processes comparable to commercial sputtered TCOs. We foresee that the potential of buffer-free devices will only be realized when more research activities are devoted to this direction.

ACKNOWLEDGMENTS

This work was supported by the King Abdullah University of Science and Technology (KAUST) Office of Sponsored Research (OSR) under award numbers OSR-2019-CARF/CCF-3097 and OSR-2019-CRG-4093, from the Spanish Ministry of Science, Innovation, and Universities (MICIU, MAT2017-88821-R, CEX2019-000919-M), and the Comunitat Valenciana (IDIFEDER/2018/061 and PROMETEU/2020/077). A.P. acknowledges his Grisolia grant from the Comunitat Valenciana GRISOLIAP/2020/134. Y.S. and M.M.-M. acknowledge support from the Solar Era Net CUSTCO project (project number SOL18001). Figures 1 and 2 were created by Heno Hwang, scientific illustrator at King Abdullah University of Science and Technology (KAUST).

AUTHOR CONTRIBUTIONS

Conceptualization, E.A.; writing – original draft, E.A., C.A., and M.A.Y.; writing – review & editing, E.A., C.A., Y.S., M.A.Y., K.P.S.Z., A.P., Y.F., and T.G.A.; funding acquisition, T.D.A., H.J.B., M.M.-M., and S.D.W.; supervision, T.D.A., H.J.B., M.M.-M., and S.D.W.

DECLARATION OF INTERESTS

The authors declare no competing interests.

REFERENCES

1. Kasap, S., and Capper, P. (2017). Springer Handbook of Electronic and Photonic Materials, *2*, Edition (Springer International Publishing).

2. Liu, L., Cao, K., Chen, S., and Huang, W. (2020). Toward see-through optoelectronics: transparent light-emitting diodes and solar cells. Adv. Opt. Mater. *8*, 2001122. https://doi.org/10.1002/adom.202001122.

3. Allen, T.G., Bullock, J., Yang, X., Javey, A., and De Wolf, S. (2019). Passivating contacts for crystalline silicon solar cells. Nat. Energy *4*, 914–928. https://doi.org/10.1038/s41560-019-0463-6.

4. Shah, A., Schade, H., Vanecek, M., Meier, J., Vallat-Sauvain, E., Wyrsch, N., Kroll, U., Droz, C., and Bailat, J. (2004). Thin-film silicon solar cell technology. Prog. Photovolt Res. Appl. *12*, 113–142. https://doi.org/10.1002/pip.533.

5. Zuo, C., Bolink, H.J., Han, H., Huang, J., Cahen, D., and Ding, L. (2016). Advances in perovskite solar cells. Adv. Sci. *3*, 1500324. https://doi.org/10.1002/advs.201500324.

6. Hoppe, H., and Sariciftci, N.S. (2004). Organic solar cells: an overview. J. Mater. Res. *19*, 1924–1945. https://doi.org/10.1557/JMR.2004.0252.

7. Kramer, I.J., and Sargent, E.H. (2014). The architecture of colloidal quantum dot solar cells: materials to devices. Chem. Rev. *114*, 863–882. https://doi.org/10.1021/cr400299t.

8. Kalyani, N.T., and Dhoble, S. (2012). Organic light emitting diodes: energy saving lighting technology—a review. Renew. Sustain. Energy Rev. *16*, 2696–2723. https://doi.org/10.1016/j.rser.2012.02.021.

9. Dai, X., Deng, Y., Peng, X., and Jin, Y. (2017). Quantum-dot light-emitting diodes for large-area displays: towards the dawn of commercialization. Adv. Mater. *29*, 1607022. https://doi.org/10.1002/adma.201607022.

10. Morales-Masis, M., De Wolf, S., Woods-Robinson, R., Ager, J.W., and Ballif, C. (2017). Transparent electrodes for efficient optoelectronics. Adv. Electron. Mater. *3*, 1600529. https://doi.org/10.1002/aelm.201600529.

11. Bush, K.A., Bailie, C.D., Chen, Y., Bowring, A.R., Wang, W., Ma, W., Leijtens, T., Moghadam, F., and McGehee, M.D. (2016). Thermal and environmental stability of semi-transparent perovskite solar cells for tandems

enabled by a solution-processed nanoparticle buffer layer and sputtered ITO electrode. Adv. Mater. *28*, 3937–3943. https://doi.org/10.1002/adma.201505279.

12. Werner, J., Dubuis, G., Walter, A., Löper, P., Moon, S.-J., Nicolay, S., Morales-Masis, M., De Wolf, S., Niesen, B., and Ballif, C. (2015). Sputtered rear electrode with broadband transparency for perovskite solar cells. Sol. Energy Mater. Sol. Cells *141*, 407–413. https://doi.org/10.1016/j.solmat.2015.06.024.

13. Aydin, E., De Bastiani, M., Yang, X., Sajjad, M., Aljamaan, F., Smirnov, Y., Hedhili, M.N., Liu, W., Allen, T.G., Xu, L., et al. (2019). Zr-doped ındium oxide (IZRO) transparent electrodes for perovskite-based tandem solar cells. Adv. Funct. Mater. *29*, 1901741. https://doi.org/10.1002/adfm.201901741.

14. Jäger, T., Romanyuk, Y., Nishiwaki, S., Bissig, B., Pianezzi, F., Fuchs, P., Gretener, C., Döbeli, M., and Tiwari, A. (2015). Hydrogenated indium oxide window layers for high-efficiency Cu(In,Ga)Se2 solar cells. J. Appl. Phys. *117*, 205301. https://doi.org/10.1063/1.4921445.

15. Demaurex, B., De Wolf, S., Descoeudres, A., Charles Holman, Z., and Ballif, C. (2012). Damage at hydrogenated amorphous/crystalline silicon interfaces by indium tin oxide overlayer sputtering. Appl. Phys. Lett. *101*, 171604. https://doi.org/10.1063/1.4764529.

16. Kanda, H., Uzum, A., Baranwal, A.K., Peiris, T.A.N., Umeyama, T., Imahori, H., Segawa, H., Miyasaka, T., and Ito, S. (2016). Analysis of sputtering damage on I–V curves for perovskite solar Cells and simulation with reversed diode model. J. Phys. Chem. C *120*, 28441–28447. https://doi.org/10.1021/acs.jpcc.6b09219.

17. Fan, Q.H., Deng, M., Liao, X., and Deng, X. (2009). Damage mechanisms in thin film solar cells during sputtering deposition of transparent conductive coatings. J. Appl. Phys. *105*, 33304. https://doi.org/10.1063/1.3074328.

18. Zhang, S., Liu, Z., Zhang, W., Jiang, Z., Chen, W., Chen, R., Huang, Y., Yang, Z., Zhang, Y., Han, L., and Chen, W. (2020). Barrier designs in perovskite solar cells for long-term stability. Adv. Energy Mater. *10*, 2001610. https://doi.org/10.1002/aenm.202001610.

19. Ramírez Quiroz, C.O., Shen, Y., Salvador, M., Forberich, K., Schrenker, N., Spyropoulos, G.D., Heumüller, T., Wilkinson, B., Kirchartz, T., Spiecker, E., et al. (2018). Balancing electrical and optical losses for efficient 4-terminal Si–perovskite solar cells with solution processed percolation electrodes. J. Mater. Chem. A *6*, 3583–3592. https://doi.org/10.1039/C7TA10945H.

20. Gaynor, W., Burkhard, G.F., McGehee, M.D., and Peumans, P. (2011). Smooth nanowire/polymer composite transparent electrodes. Adv. Mater. *23*, 2905–2910. https://doi.org/10.1002/adma.201100566.

21. Yu, L., Shearer, C., and Shapter, J. (2016). Recent development of carbon nanotube transparent conductive films. Chem. Rev. *116*, 13413–13453. https://doi.org/10.1021/acs.chemrev.6b00179.

22. Hofmann, A.I., Cloutet, E., and Hadziioannou, G. (2018). Materials for transparent electrodes: from metal oxides to organic alternatives. Adv. Electron. Mater. *4*, 1700412. https://doi.org/10.1002/aelm.201700412.

23. Kim, S., and Lee, J.-L. (2012). Design of dielectric/metal/dielectric transparent electrodes for flexible electronics. J. Photon. Energy *2*, 021215. https://doi.org/10.1117/1.JPE.2.021215.

24. Jin, H., Tao, C., Velusamy, M., Aljada, M., Zhang, Y., Hambsch, M., Burn, P.L., and Meredith, P. (2012). Efficient, large area ITO-and-PEDOT-free organic solar cell sub-modules. Adv. Mater. *24*, 2572–2577. https://doi.org/10.1002/adma.201104896.

25. Giuliano, G., Cataldo, S., Scopelliti, M., Principato, F., Chillura Martino, D., Fiore, T., and Pignataro, B. (2019). Nonprecious copper-based transparent top electrode via seed layer–assisted thermal evaporation for high-performance semitransparent n-i-p perovskite solar cells. Adv. Mater. Technol. *4*, 1800688. https://doi.org/10.1002/admt.201800688.

26. Hong, K., Kim, K., Kim, S., Lee, I., Cho, H., Yoo, S., Choi, H.W., Lee, N.-Y., Tak, Y.-H., and Lee, J.-L. (2011). Optical properties of WO3/Ag/WO3 multilayer as transparent cathode in top-emitting organic light emitting diodes. J. Phys. Chem. C *115*, 3453–3459. https://doi.org/10.1021/jp109943b.

27. Morales-Masis, M., Dauzou, F., Jeangros, Q., Dabirian, A., Lifka, H., Gierth, R., Ruske, M., Moet, D., Hessler-Wyser, A., and Ballif, C. (2016). An Indium-free anode for large-area flexible OLEDs: defect-free transparent conductive zinc tin oxide. Adv. Funct. Mater. *26*, 384–392. https://doi.org/10.1002/adfm.201503753.

28. Cao, W., Li, J., Chen, H., and Xue, J. (2014). Transparent electrodes for organic optoelectronic devices: a review. J. Photon. Energy *4*, 040990. https://doi.org/10.1117/1.JPE.4.040990.

29. Moualkia, H., Hariech, S., and Aida, M. (2009). Structural and optical properties of CdS thin films grown by chemical bath deposition. Thin Solid Films *518*, 1259–1262. https://doi.org/10.1016/j.tsf.2009.04.067.

30. Jørgensen, M., Norrman, K., and Krebs, F.C. (2008). Stability/degradation of polymer solar cells. Sol. Energy Mater. Sol. Cells *92*, 686–714. https://doi.org/10.1016/j.solmat.2008.01.005.

31. Rösch, R., Tanenbaum, D.M., Jørgensen, M., Seeland, M., Bärenklau, M., Hermenau, M., Voroshazi, E., Lloyd, M.T., Galagan, Y., Zimmermann, B., et al. (2012). Investigation of the degradation mechanisms of a variety of organic photovoltaic devices by combination of imaging techniques—the ISOS-3 inter-laboratory collaboration. Energy Environ. Sci. *5*, 6521–6540. https://doi.org/10.1039/C2EE03508A.

32. Wang, X., Zhang, X., Sun, L., Lee, D., Lee, S., Wang, M., Zhao, J., Shao-Horn, Y., Dincă, M., and Palacios, T. (2018). High electrical conductivity and carrier mobility in oCVD PEDOT thin films by engineered crystallization and acid treatment. Sci. Adv. *4*, eaat5780. https://doi.org/10.1126/sciadv.aat5780.

33. Morales-Masis, M., De Nicolas, S.M., Holovsky, J., De Wolf, S., and Ballif, C. (2015). Low-temperature high-mobility amorphous IZO for silicon heterojunction solar cells. IEEE J. Photovoltaics *5*, 1340–1347. https://doi.org/10.1109/JPHOTOV.2015.2450993.

34. Ellmer, K., and Welzel, T. (2012). Reactive magnetron sputtering of transparent conductive oxide thin films: role of energetic particle (ion) bombardment. J. Mater. Res. *27*, 765–779. https://doi.org/10.1557/jmr.2011.428.

35. Welzel, T., and Ellmer, K. (2012). Negative oxygen ion formation in reactive magnetron sputtering processes for transparent conductive oxides. J. Vacuum Sci. Technol. A *30*, 061306. https://doi.org/10.1116/1.4762815.

36. Ellmer, K. (2008). Magnetron discharges for thin film deposition. In Low Temperature Plasmas. Fundamentals, Technologies and Techniques, R. Hippler, H. Kersten, M. Schmidt, and K.H. Schoenbach, eds. (Wiley-VCH), pp. 675–715.

37. Lieberman, M.A., and Lichtenberg, A.J. (2005). Principles of Plasma Discharges and Materials Processing, 2nd Edition (John Wiley & Sons).

38. Jagt, R.A., Huq, T.N., Hill, S.A., Thway, M., Liu, T., Napari, M., Roose, B., Gałkowski, K., Li, W., Lin, S.F., et al. (2020). Rapid vapor-phase deposition of high-mobility p-type buffer layers on perovskite photovoltaics for efficient semitransparent devices. ACS Energy Lett. *5*, 2456–2465. https://doi.org/10.1021/acsenergylett.0c00763.

39. Carcia, P.F., McLean, R.S., Reilly, M.H., Li, Z.G., Pillione, L.J., and Messier, R.F. (2003). Influence of energetic bombardment on stress, resistivity, and microstructure of indium tin oxide films grown by radio frequency magnetron sputtering on flexible polyester substrates. J. Vacuum Sci. Technol. A *21*, 745–751. https://doi.org/10.1116/1.1566789.

40. Jia, J., Torigoshi, Y., and Shigesato, Y. (2013). In situ analyses on negative ions in the indium-gallium-zinc oxide sputtering process. Appl. Phys. Lett. *103*, 013501. https://doi.org/10.1063/1.4812668.

41. Mahieu, S., Leroy, W., Van Aeken, K., and Depla, D. (2009). Modeling the flux of high energy negative ions during reactive magnetron sputtering. J. Appl. Phys. *106*, 093302. https://doi.org/10.1063/1.3247545.

42. Nathan, S.S., Rao, G.M., and Mohan, S. (1998). Transport of sputtered atoms in facing targets sputtering geometry: a numerical simulation study. J. Appl. Phys. *84*, 564–571. https://doi.org/10.1063/1.368061.

43. Kim, H.-K., Kim, D.-G., Lee, K.-S., Huh, M.-S., Jeong, S.H., Kim, K.I., and Seong, T.-Y. (2005). Plasma damage-free sputtering of indium tin oxide cathode layers for top-emitting organic light-emitting diodes. Appl. Phys. Lett. *86*, 183503. https://doi.org/10.1063/1.1923182.

44. Suemori, K., Hoshino, S., Ibaraki, N., and Kamata, T. (2017). Effect of positively charged

particles on sputtering damage of organic electro-luminescent diodes with Mg:Ag alloy electrodes fabricated by facing target sputtering. AIP Adv. *7*, 045014. https://doi.org/10.1063/1.4981799.

45. Kim, J.-G., Lee, J.-H., Na, S.-I., Lee, H.H., Kim, Y., and Kim, H.-K. (2020). Semi-transparent perovskite solar cells with directly sputtered amorphous InZnSnO top cathodes for building integrated photovoltaics. Org. Electron. *78*, 105560. https://doi.org/10.1016/j.orgel.2019.105560.

46. Standard Bond Energies and Bond Dissociation Energies. https://web.archive.org/web/20160829213457/ http://www.cem.msu.edu/~reusch/OrgPage/bndenrgy.htm#dissbe.

47. Griffith, M.J., Cooling, N.A., Vaughan, B., O'Donnell, K.M., Al-Mudhaffer, M.F., Al-Ahmad, A., Noori, M., Almyahi, F., Belcher, W.J., and Dastoor, P.C. (2015). Roll-to-roll sputter coating of aluminum cathodes for large-scale fabrication of organic photovoltaic devices. Energy Technol. *3*, 428–436. https://doi.org/10.1002/ente.201402174.

48. Matsuo, N., Hironiwa, D., Chantana, J., Sakai, N., Kato, T., Sugimoto, H., and Minemoto, T. (2015). Evaluation of sputtering damage in Cu2ZnSn (S, Se) 4 solar cells with CdS and (Cd, Zn) S buffer layers by photoluminescence measurement. Jpn. J. Appl. Phys. *54*, 042302. https://doi.org/10.7567/JJAP.54.042302.

49. Burst, J.M., Duenow, J.N., Albin, D.S., Colegrove, E., Reese, M.O., Aguiar, J.A., Jiang, C.S., Patel, M.K., Al-Jassim, M.M., Kuciauskas, D., et al. (2016). CdTe solar cells with open-circuit voltage breaking the 1 V barrier. Nat. Energy *1*, 16015. https://doi.org/10.1038/nenergy.2016.15.

50. Bush, K.A., Palmstrom, A.F., Yu, Z.J., Boccard, M., Cheacharoen, R., Mailoa, J.P., McMeekin, D.P., Hoye, R.L.Z., Bailie, C.D., Leijtens, T., et al. (2017). 23.6%-efficient monolithic perovskite/silicon tandem solar cells with improved stability. Nat. Energy *2*, 17009. https://doi.org/10.1038/nenergy.2017.9.

51. Sahli, F., Werner, J., Kamino, B.A., Bräuninger, M., Monnard, R., Paviet-Salomon, B., Barraud, L., Ding, L., Diaz Leon, J.J., Sacchetto, D., et al. (2018). Fully textured monolithic perovskite/silicon tandem solar cells with 25.2% power conversion efficiency. Nat. Mater. *17*, 820–826. https://doi.org/10.1038/s41563-018-0115-4.

52. Aydin, E., Allen, T.G., De Bastiani, M., Xu, L., Ávila, J., Salvador, M., Van Kerschaver, E., and De Wolf, S. (2020). Interplay between temperature and bandgap energies on the outdoor performance of perovskite/silicon tandem solar cells. Nat. Energy *5*, 851–859. https://doi.org/10.1038/s41560-020-00687-4.

53. Al-Ashouri, A., Köhnen, E., Li, B., Magomedov, A., Hempel, H., Caprioglio, P., Márquez, J.A., Morales Vilches, A.B., Kasparavicius, E., Smith, J.A., et al. (2020). Monolithic perovskite/silicon tandem solar cell with >29% efficiency by enhanced hole extraction. Science *370*, 1300–1309. https://doi.org/10.1126/science.abd4016.

54. Saive, R. (2019). S-shaped current–voltage characteristics in solar cells: a review. IEEE J. Photovoltaics *9*, 1477–1484. https://doi.org/10.1109/JPHOTOV.2019.2930409.

55. Najafi, M., Zardetto, V., Zhang, D., Koushik, D., Dörenkämper, M.S., Creatore, M., Andriessen, R., Poodt, P., and Veenstra, S. (2018). Highly efficient and stable semi-transparent p-i-n planar perovskite solar cells by atmospheric pressure spatial atomic layer deposited ZnO. Sol. RRL *2*, 1800147. https://doi.org/10.1002/solr.201800147.

56. Ahlswede, E., Hanisch, J., and Powalla, M. (2007). Influence of cathode sputter deposition on organic solar cells. Appl. Phys. Lett. *90*, 063513. https://doi.org/10.1063/1.2472719.

57. Jouane, Y., Colis, S., Schmerber, G., Kern, P., Dinia, A., Heiser, T., and Chapuis, Y.-A. (2011). Room temperature ZnO growth by RF magnetron sputtering on top of photoactive P3HT: PCBM for organic solar cells. J. Mater. Chem. *21*, 1953–1958. https://doi.org/10.1039/C0JM02354J.

58. Altinkaya, C., Aydin, E., Ugur, E., Isikgor, F.H., Subbiah, A.S., De Bastiani, M., Liu, J., Babayigit, A., Allen, T.G., and Laquai, F. (2021). Tin oxide electron-selective layers for efficient, stable, and scalable perovskite solar cells. Adv. Mater. *33*, 2005504. https://doi.org/10.1002/adma.202005504.

59. Hu, Z., Wang, Z., An, Q., and Zhang, F. (2020). Semitransparent polymer solar cells with 12.37% efficiency and 18.6% average visible transmittance. Sci. Bull. *65*, 131–137. https://doi.org/10.1016/j.scib.2019.09.016.

60. Illiberi, A., Kudlacek, P., Smets, A., Creatore, M., and Van De Sanden, M. (2011). Effect of ion bombardment on the a-Si: H based surface passivation of c-Si surfaces. Appl. Phys. Lett. *98*, 242115. https://doi.org/10.1063/1.3601485.

61. Hou, Y., Aydin, E., De Bastiani, M., Xiao, C., Isikgor, F.H., Xue, D.-J., Chen, B., Chen, H., Bahrami, B., and Chowdhury, A.H. (2020). Efficient tandem solar cells with solution-processed perovskite on textured crystalline silicon. Science *367*, 1135–1140. https://doi.org/10.1126/science.aaz3691.

62. Linss, V., Bivour, M., Iwata, H., and Ortner, K. (2019). Comparison of low damage sputter deposition techniques to enable the application of very thin a-Si passivation films. AIP Conf. Proc. *2147*, 040009. https://doi.org/10.1063/1.5123836.

63. Demaurex, B., Seif, J.P., Smit, S., Macco, B., Kessels, W., Geissbühler, J., De Wolf, S., and Ballif, C. (2014). Atomic-layer-deposited transparent electrodes for silicon heterojunction solar cells. IEEE J. Photovoltaics *4*, 1387–1396. https://doi.org/10.1109/JPHOTOV.2014.2344771.

64. Sugiyama, M., Sakakura, H., Chang, S.-W., and Itagaki, M. (2014). Investigation of sputtering damage around pn interfaces of Cu(In, Ga)Se2 solar cells by impedance spectroscopy. Electrochim. Acta *131*, 236–239. https://doi.org/10.1016/j.electacta.2014.04.058.

65. Rey, G., Paduthol, A., Sun, K., Nagle, T., Poplavskyy, D., Escalant, V.S., Melchiorre, M., Siebentritt, S., Abbott, M., and Trupke, T. (2019). Photoluminescence-based method for imaging buffer layer thickness in CIGS solar cells. IEEE J. Photovoltaics *10*, 181–187. https://doi.org/10.1109/JPHOTOV.2019.2950630.

66. Trupke, T., Bardos, R., Schubert, M., and Warta, W. (2006). Photoluminescence imaging of silicon wafers. Appl. Phys. Lett. *89*, 044107. https://doi.org/10.1063/1.2234747.

67. Lee, Y.S., Gershon, T., Todorov, T.K., Wang, W., Winkler, M.T., Hopstaken, M., Gunawan, O., and Kim, J. (2016). Atomic layer deposited aluminum oxide for interface passivation of Cu2ZnSn (S, Se) 4 thin-film solar cells. Adv. Energy Mater. *6*, 1600198. https://doi.org/10.1002/aenm.201600198.

68. Johnston, S., Repins, I., Call, N., Sundaramoorthy, R., Jones, K.M., and To, B. (2010). Applications of Imaging Techniques to Si, Cu (In, Ga) Se 2, and CdTe and Correlation to Solar Cell Parameters. 2010 35th IEEE Photovoltaic Specialists Conference, Honolulu, HI, USA. (IEEE), pp. 001727-001732I. https://doi.org/10.1109/PVSC.2010.5616123.

69. Schubert, M.C., Mundt, L.E., Walter, D., Fell, A., and Glunz, S.W. (2020). Spatially resolved performance analysis for perovskite solar cells. Adv. Energy Mater. *10*, 1904001. https://doi.org/10.1002/aenm.201904001.

70. El-Hajje, G., Momblona, C., Gil-Escrig, L., Ávila, J., Guillemot, T., Guillemoles, J.-F., Sessolo, M., Bolink, H.J., and Lombez, L. (2016). Quantification of spatial inhomogeneity in perovskite solar cells by hyperspectral luminescence imaging. Energy Environ. Sci. *9*, 2286–2294. https://doi.org/10.1039/C6EE00462H.

71. Klein, A., Körber, C., Wachau, A., Säuberlich, F., Gassenbauer, Y., Harvey, S.P., Proffit, D.E., and Mason, T.O. (2010). Transparent conducting oxides for photovoltaics: Manipulation of fermi level, work function and energy band alignment. Materials *3*, 4892–4914. https://doi.org/10.3390/ma3114892.

72. Krishnakumar, V., Klein, A., and Jaegermann, W. (2013). Studies on CdTe solar cell front contact properties using X-ray photoelectron spectroscopy. Thin Solid Films *545*, 548–557. https://doi.org/10.1016/j.tsf.2013.08.083.

73. Liao, L.S., Hung, L.S., Chan, W.C., Ding, X.M., Sham, T.K., Bello, I., Lee, C.S., and Lee, S.T. (1999). Ion-beam-induced surface damages on tris-(8-hydroxyquinoline) aluminum. Appl. Phys. Lett. *75*, 1619–1621. https://doi.org/10.1063/1.124773.

74. Gassenbauer, Y., Wachau, A., and Klein, A. (2009). Chemical and electronic properties of the ITO/Al2O3 interface. Phys. Chem. Chem. Phys. *11*, 3049–3054. https://doi.org/10.1039/B822848E.

75. Gassmann, J.r., Yampolskii, S.V., Genenko, Y.A., Reusch, T.C., and Klein, A. (2016). Functional interfaces for transparent organic electronic devices: Consistent description of charge injection by combining in situ XPS and current voltage measurements with self-consistent modeling. J. Phys. Chem. C *120*,

10466–10475. https://doi.org/10.1021/acs.jpcc.6b02567.

76. Gil, T.H., May, C., Scholz, S., Franke, S., Toerker, M., Lakner, H., Leo, K., and Keller, S. (2010). Origin of damages in OLED from Al top electrode deposition by DC magnetron sputtering. Org. Electron. *11*, 322–331. https://doi.org/10.1016/j.orgel.2009.11.011.

77. Lei, H., Wang, M., Hoshi, Y., Uchida, T., Kobayashi, S., and Sawada, Y. (2013). Comparative studies on damages to organic layer during the deposition of ITO films by various sputtering methods. Appl. Surf. Sci. *285*, 389–394. https://doi.org/10.1016/j.apsusc.2013.08.065.

78. Lei, H., Ichikawa, K., Wang, M., Hoshi, Y., Uchida, T., and Sawada, Y. (2008). Investigation of low-damage sputter-deposition of ITO films on organic emission layer. IEICE Trans. Electron. *91*, 1658–1662. https://doi.org/10.1093/ietele/e91-c.10.1658.

79. Wang, W., Peng, H., and Chen, S. (2016). Highly transparent quantum-dot light-emitting diodes with sputtered indium-tin-oxide electrodes. J. Mater. Chem. C *4*, 1838–1841. https://doi.org/10.1039/C5TC04223B.

80. Choi, M.K., Yang, J., Kim, D.C., Dai, Z., Kim, J., Seung, H., Kale, V.S., Sung, S.J., Park, C.R., and Lu, N. (2018). Extremely vivid, highly transparent, and ultrathin quantum dot light-emitting diodes. Adv. Mater. *30*, 1703279. https://doi.org/10.1002/adma.201703279.

81. Jung, G.H., Hong, K., Dong, W.J., Kim, S., and Lee, J.L. (2011). BCP/Ag/MoO3 transparent cathodes for organic photovoltaics. Adv. Energy Mater. *1*, 1023–1028. https://doi.org/10.1002/aenm.201100411.

82. Burschka, J., Pellet, N., Moon, S.-J., Humphry-Baker, R., Gao, P., Nazeeruddin, M.K., and Grätzel, M. (2013). Sequential deposition as a route to high-performance perovskite-sensitized solar cells. Nature *499*, 316–319. https://doi.org/10.1038/nature12340.

83. Fu, F., Feurer, T., Weiss, T.P., Pisoni, S., Avancini, E., Andres, C., Buecheler, S., and Tiwari, A.N. (2016). High-efficiency inverted semi-transparent planar perovskite solar cells in substrate configuration. Nat. Energy *2*, 16190. https://doi.org/10.1038/nenergy.2016.190.

84. Zhu, Z., Bai, Y., Liu, X., Chueh, C.C., Yang, S., and Jen, A.K.Y. (2016). Enhanced efficiency and stability of inverted perovskite solar cells using highly crystalline SnO2 nanocrystals as the robust electron-transporting layer. Adv. Mater. *28*, 6478–6484. https://doi.org/10.1002/adma.201600619.

85. McMeekin, D.P., Sadoughi, G., Rehman, W., Eperon, G.E., Saliba, M., Hörantner, M.T., Haghighirad, A., Sakai, N., Korte, L., Rech, B., et al. (2016). A mixed-cation lead mixed-halide perovskite absorber for tandem solar cells. Science *351*, 151–155. https://doi.org/10.1126/science.aad5845.

86. Kuwano, K., Ogo, H., Chikamatsu, M., Yoshida, Y., Watanabe, Y., and Nishikawa, E. (2019). Effects on p-type buffer layers for semitransparent organic photovoltaics using indium zinc oxide transparent electrode. Jpn. J. Appl. Phys. *59*, SDDD04. https://doi.org/10.7567/1347-4065/ab4eb9.

87. Han, C.-Y., Lee, K.-H., Kim, M.-S., Shin, J.-W., Kim, J.S., Hwang, J.-H., Kim, T., Oh, M.S., Kim, J., and Do, Y.R. (2017). Solution-processed fabrication of highly transparent mono-and tri-colored quantum dot-light-emitting diodes. Org. Electron. *45*, 145–150. https://doi.org/10.1016/j.orgel.2017.03.012.

88. Zhang, H., and Chen, S. (2019). An ZnMgO: PVP inorganic–organic hybrid electron transport layer: towards efficient bottom-emission and transparent quantum dot light-emitting diodes. J. Mater. Chem. C *7*, 2291–2298. https://doi.org/10.1039/C8TC06121A.

89. Zhou, Y., Li, X., and Lin, H. (2020). To be higher and stronger—metal oxide electron transport materials for perovskite solar cells. Small *16*, 1902579. https://doi.org/10.1002/smll.201902579.

90. Zanoni, K.P., Perez-del-Rey, D., Dreessen, C., Hernández-Fenollosa, M.A., De Camargo, A.S., Sessolo, M., Boix, P.P., and Bolink, H.J. (2020). Use of hydrogen molybdenum bronze in vacuum-deposited perovskite solar cells. Energy Technol. *8*, 1900734. https://doi.org/10.1002/ente.201900734.

91. Kim, D., Jung, H.J., Park, I.J., Larson, B.W., Dunfield, S.P., Xiao, C., Kim, J., Tong, J., Boonmongkolras, P., Ji, S.G., et al. (2020). Efficient, stable silicon tandem cells enabled by anion-engineered wide-bandgap perovskites. Science *368*, 155–160. https://doi.org/10.1126/science.aba3433.

92. Kim, J.-H., and Park, J.-W. (2017). Designing an electron-transport layer for highly efficient, reliable, and solution-processed organic light-emitting diodes. J. Mater. Chem. C *5*, 3097–3106. https://doi.org/10.1039/C7TC00488E.

93. Zhou, Y., Fuentes-Hernandez, C., Shim, J., Meyer, J., Giordano, A.J., Li, H., Winget, P., Papadopoulos, T., Cheun, H., Kim, J., et al. (2012). A universal method to produce low–work function electrodes for organic electronics. Science *336*, 327–332. https://doi.org/10.1126/science.1218829.

94. Raiford, J.A., Boyd, C.C., Palmstrom, A.F., Wolf, E.J., Fearon, B.A., Berry, J.J., McGehee, M.D., and Bent, S.F. (2019). Enhanced nucleation of atomic layer deposited contacts ımproves operational stability of perovskite solar cells in air. Adv. Energy Mater. *9*, 1902353. https://doi.org/10.1002/aenm.20190235.

95. Han, J.-f., Liao, C., Cha, L.-m., Jiang, T., Xie, H.-m., Zhao, K., and Besland, M.-P. (2014). TEM and XPS studies on CdS/CIGS interfaces. J. Phys. Chem. Sol. *75*, 1279–1283. https://doi.org/10.1016/j.jpcs.2014.06.002.

96. Naghavi, N., Abou-Ras, D., Allsop, N., Barreau, N., Bücheler, S., Ennaoui, A., Fischer, C.H., Guillen, C., Hariskos, D., Herrero, J., et al. (2010). Buffer layers and transparent conducting oxides for chalcopyrite Cu(In,Ga)(S,Se)2 based thin film photovoltaics: present status and current developments. Prog. Photovolt: Res. Appl. *18*, 411–433. https://doi.org/10.1002/pip.955.

97. Mughal, M.A., Engelken, R., and Sharma, R. (2015). Progress in indium (III) sulfide (In2S3) buffer layer deposition techniques for CIS, CIGS, and CdTe-based thin film solar cells. Sol. Energy *120*, 131–146. https://doi.org/10.1016/j.solener.2015.07.028.

98. Gour, K.S., Parmar, R., Kumar, R., and Singh, V.N. (2020). Cd-free Zn (O, S) as alternative buffer layer for chalcogenide and kesterite based thin films solar cells: a review. J. Nanosci. Nanotechnol. *20*, 3622–3635. https://doi.org/10.1166/jnn.2020.17537.

99. Nakamura, M., Yamaguchi, K., Kimoto, Y., Yasaki, Y., Kato, T., and Sugimoto, H. (2019). Cd-free Cu (In, Ga)(Se, S)2 thin-film solar cell with record efficiency of 23.35%. IEEE J. Photovoltaics *9*, 1863–1867. https://doi.org/10.1109/JPHOTOV.2019.2937218.

100. Feurer, T., Reinhard, P., Avancini, E., Bissig, B., Löckinger, J., Fuchs, P., Carron, R., Weiss, T.P., Perrenoud, J., and Stutterheim, S. (2017). Progress in thin film CIGS photovoltaics–research and development, manufacturing, and applications. Prog. Photovolt: Res. Appl. *25*, 645–667. https://doi.org/10.1002/pip.2811.

101. Mane, R., and Lokhande, C. (2000). Chemical deposition method for metal chalcogenide thin films. Mater. Chem. Phys. *65*, 1–31. https://doi.org/10.1016/S0254-0584(00)00217-0.

102. Hashimoto, Y., Kohara, N., Negami, T., Nishitani, N., and Wada, T. (1998). Chemical bath deposition of CdS buffer layer for GIGS solar cells. Sol. Energy Mater. Sol. Cells *50*, 71–77. https://doi.org/10.1016/S0927-0248(97)00124-4.

103. Rakhshani, A.E., and Al-Azab, A.S. (2000). Characterization of CdS films prepared by chemical-bath deposition. J. Phys. Condens. Matter *12*, 8745–8755. https://doi.org/10.1088/0953-8984/12/40/316.

104. Nakada, T., Mizutani, M., Hagiwara, Y., and Kunioka, A. (2001). High-efficiency Cu(In,Ga)Se2 thin-film solar cells with a CBD-ZnS buffer layer. Sol. Energy Mater. Sol. Cells *67*, 255–260. https://doi.org/10.1016/S0927-0248(00)00289-0.

105. Nakada, T., and Mizutani, M. (2002). 18% Efficiency Cd-Free Cu(In, Ga)Se2 thin-film solar cells fabricated using chemical bath deposition (CBD)-ZnS buffer layers. Jpn. J. Appl. Phys. *41*, L165–L167. https://doi.org/10.1143/jjap.41.l165.

106. Yoo, J.J., Seo, G., Chua, M.R., Park, T.G., Lu, Y., Rotermund, F., Kim, Y.-K., Moon, C.S., Jeon, N.J., Correa-Baena, J.-P., et al. (2021). Efficient perovskite solar cells via improved carrier management. Nature *590*, 587–593. https://doi.org/10.1038/s41586-021-03285-w.

107. Mattox, D.M. (2010). Vacuum evaporation and vacuum deposition. In Handbook of Physical Vapor Deposition (PVD) Processing, D.M. Mattox, ed. (William Andrew Publishing)), pp. 195–235. https://doi.org/10.1016/B978-0-8155-2037-5.00006-X.

108. Dewi, H.A., Wang, H., Li, J., Thway, M., Sridharan, R., Stangl, R., Lin, F., Aberle, A.G., Mathews, N., Bruno, A., and Mhaisalkar, S. (2019). Highly efficient semitransparent

perovskite solar cells for four terminal perovskite-silicon tandems. ACS Appl. Mater. Interfaces *11*, 34178–34187. https://doi.org/10.1021/acsami.9b13145.

109. Burrows, P.E., Gu, G., Forrest, S.R., Vicenzi, E.P., and Zhou, T.X. (2000). Semitransparent cathodes for organic light emitting devices. J. Appl. Phys. *87*, 3080–3085. https://doi.org/10.1063/1.372303.

110. Hanisch, J., Ahlswede, E., and Powalla, M. (2007). Contacts for semitransparent organic solar cells. EPJ Appl. Phys. *37*. https://doi.org/10.1051/epjap:2007041.

111. Bulovic, V., Gu, G., Burrows, P.E., Forrest, S.R., and Thompson, M.E. (1996). Transparent light-emitting devices. Nature *380*, *29*. https://doi.org/10.1038/380029a0.

112. Yun, J. (2017). Ultrathin metal films for transparent electrodes of flexible optoelectronic devices. Adv. Funct. Mater. *27*, 1606641. https://doi.org/10.1002/adfm.201606641.

113. Yang, D., Zhang, X., Hou, Y., Wang, K., Ye, T., Yoon, J., Wu, C., Sanghadasa, M., Liu, S.F., and Priya, S. (2021). 28.3%-efficiency perovskite/silicon tandem solar cell by optimal transparent electrode for high efficient semitransparent top cell. Nano Energy *84*, 105934. https://doi.org/10.1016/j.nanoen.2021.105934.

114. Hordequin, C., Tromson, D., Brambilla, A., Bergonzo, P., and Foulon, F. (2001). Strong impact of X-ray radiation associated with electron beam metallization of diamond devices. J. Appl. Phys. *90*, 2533–2537. https://doi.org/10.1063/1.1338515.

115. Sahli, F., Kamino, B.A., Werner, J., Bräuninger, M., Paviet-Salomon, B., Barraud, L., Monnard, R., Seif, J.P., Tomasi, A., Jeangros, Q., et al. (2018). Improved optics in monolithic perovskite/silicon tandem solar cells with a nanocrystalline silicon recombination junction. Adv. Energy Mater. *8*, 1701609. https://doi.org/10.1002/aenm.201701609.

116. Wu, Y., Yan, D., Peng, J., Duong, T., Wan, Y., Phang, S.P., Shen, H., Wu, N., Barugkin, C., Fu, X., et al. (2017). Monolithic perovskite/silicon-homojunction tandem solar cell with over 22% efficiency. Energy Environ. Sci. *10*, 2472–2479. https://doi.org/10.1039/C7EE02288C.

117. Zhao, D., Wang, C., Song, Z., Yu, Y., Chen, C., Zhao, X., Zhu, K., and Yan, Y. (2018). Four-terminal all-perovskite tandem solar cells achieving power conversion efficiencies exceeding 23%. ACS Energy Lett. *3*, 305–306. https://doi.org/10.1021/acsenergylett.7b01287.

118. Meyer, J., Hamwi, S., Kröger, M., Kowalsky, W., Riedl, T., and Kahn, A. (2012). Transition metal oxides for organic electronics: energetics, device physics and applications. Adv. Mater. *24*, 5408–5427. https://doi.org/10.1002/adma.201201630.

119. Cheng, M., Li, Y., Safdari, M., Chen, C., Liu, P., Kloo, L., and Sun, L. (2017). Efficient perovskite solar cells based on a solution processable nickel(II) phthalocyanine and vanadium oxide integrated hole transport layer. Adv. Energy Mater. *7*, 1602556. https://doi.org/10.1002/aenm.201602556.

120. Kim, J.H., Lee, Y.J., Jang, Y.S., Jang, J.N., Kim, D.H., Song, B.C., Lee, D.H., Kwon, S.N., and Hong, M. (2011). The effect of Ar plasma bombardment upon physical property of tungsten oxide thin film in inverted top-emitting organic light-emitting diodes. Org. Electron. *12*, 285–290. https://doi.org/10.1016/j.orgel.2010.10.023.

121. Schmidt, H., Flügge, H., Winkler, T., Bülow, T., Riedl, T., and Kowalsky, W. (2009). Efficient semitransparent inverted organic solar cells with indium tin oxide top electrode. Appl. Phys. Lett. *94*, 243302. https://doi.org/10.1063/1.3154556.

122. Qu, Y., Coburn, C., Fan, D., and Forrest, S.R. (2017). Elimination of plasmon losses and enhanced light extraction of top-emitting organic light-emitting devices using a reflective subelectrode grid. ACS Photon. *4*, 363–368. https://doi.org/10.1021/acsphotonics.6b00847.

123. Meyer, J., Winkler, T., Hamwi, S., Schmale, S., Johannes, H.-H., Weimann, T., Hinze, P., Kowalsky, W., and Riedl, T. (2008). Transparent inverted organic light-emitting diodes with a tungsten oxide buffer layer. Adv. Mater. *20*, 3839–3843. https://doi.org/10.1002/adma.200800949.

124. Gao, J., Perkins, C.L., Luther, J.M., Hanna, M.C., Chen, H.-Y., Semonin, O.E., Nozik, A.J., Ellingson, R.J., and Beard, M.C. (2011). n-Type transition metal oxide as a hole extraction layer in PbS quantum dot solar cells. Nano Lett. *11*, 3263–3266. https://doi.org/10.1021/nl2015729.

125. Maraghechi, P., Labelle, A.J., Kirmani, A.R., Lan, X., Adachi, M.M., Thon, S.M., Hoogland, S., Lee, A., Ning, Z., and Fischer, A. (2013). The donor–supply electrode enhances performance in colloidal quantum dot solar cells. ACS Nano *7*, 6111–6116. https://doi.org/10.1021/nn401918d.

126. Werner, J., Geissbühler, J., Dabirian, A., Nicolay, S., Morales-Masis, M., Wolf, S.D., Niesen, B., and Ballif, C. (2016). Parasitic absorption reduction in metal oxide-based transparent electrodes: application in perovskite solar cells. ACS Appl. Mater. Interfaces *8*, 17260–17267. https://doi.org/10.1021/acsami.6b04425.

127. Shen, H., Walter, D., Wu, Y., Fong, K.C., Jacobs, D.A., Duong, T., Peng, J., Weber, K., White, T.P., and Catchpole, K.R. (2020). Monolithic perovskite/Si tandem solar cells: pathways to over 30% efficiency. Adv. Energy Mater. *10*, 1902840. https://doi.org/10.1002/aenm.201902840.

128. Pérez-del-Rey, D., Gil-Escrig, L., Zanoni, K.P.S., Dreessen, C., Sessolo, M., Boix, P.P., and Bolink, H.J. (2019). Molecular passivation of MoO3: band alignment and protection of charge transport layers in vacuum-deposited perovskite solar cells. Chem. Mater. *31*, 6945–6949. https://doi.org/10.1021/acs.chemmater.9b01396.

129. Yamamori, A., Hayashi, S., Koyama, T., and Taniguchi, Y. (2001). Transparent organic light-emitting diodes using metal acethylacetonate complexes as an electron injective buffer layer. Appl. Phys. Lett. *78*, 3343–3345. https://doi.org/10.1063/1.1359485.

130. Ying, Z., Zhu, Y., Feng, X., Xiu, J., Zhang, R., Ma, X., Deng, Y., Pan, H., and He, Z. (2020). Sputtered indium-zinc oxide for buffer layer free semitransparent perovskite photovoltaic devices in perovskite/silicon 4T-tandem solar cells. Adv. Mater. Interfaces *8*. https://doi.org/10.1002/admi.202001604.

131. Liu, P., Liu, X., Lyu, L., Xie, H., Zhang, H., Niu, D., Huang, H., Bi, C., Xiao, Z., Huang, J., and Gao, Y. (2015). Interfacial electronic structure at the CH3NH3PbI3/MoOx interface. Appl. Phys. Lett. *106*, 193903. https://doi.org/10.1063/1.4921339.

132. Wang, M., Tang, Q., An, J., Xie, F., Chen, J., Zheng, S., Wong, K.Y., Miao, Q., and Xu, J. (2010). Performance and stability improvement of P3HT: PCBM-based solar cells by thermally evaporated chromium oxide (CrOx) interfacial layer. ACS Appl. Mater. Interfaces *2*, 2699–2702. https://doi.org/10.1021/am100541d.

133. Wan, Y., Samundsett, C., Bullock, J., Hettick, M., Allen, T., Yan, D., Peng, J., Wu, Y., Cui, J., and Javey, A. (2017). Conductive and stable magnesium oxide electron-selective contacts for efficient silicon solar cells. Adv. Energy Mater. *7*, 1601863. https://doi.org/10.1002/aenm.201601863.

134. Parthasarathy, G., Burrows, P.E., Khalfin, V., Kozlov, V.G., and Forrest, S.R. (1998). A metal-free cathode for organic semiconductor devices. Appl. Phys. Lett. *72*, 2138–2140. https://doi.org/10.1063/1.121301.

135. Bulović, V., Tian, P., Burrows, P.E., Gokhale, M.R., Forrest, S.R., and Thompson, M.E. (1997). A surface-emitting vacuum-deposited organic light emitting device. Appl. Phys. Lett. *70*, 2954. https://doi.org/10.1063/1.119260.

136. Dobbertin, T., Kroeger, M., Heithecker, D., Schneider, D., Metzdorf, D., Neuner, H., Becker, E., Johannes, H.-H., and Kowalsky, W. (2003). Inverted top-emitting organic light-emitting diodes using sputter-deposited anodes. Appl. Phys. Lett. *82*, 284–286. https://doi.org/10.1063/1.1535743.

137. Lee, J.-H., Lee, S., Kim, J.-B., Jang, J., and Kim, J.-J. (2012). A high performance transparent inverted organic light emitting diode with 1,4,5,8,9,11-hexaazatriphenylenehexacarbonitrile as an organic buffer layer. J. Mater. Chem. *22*, 15262–15266. https://doi.org/10.1039/C2JM32438E.

138. Parthasarathy, G., Gu, G., and Forrest, S.R. (1999). A full-color transparent metal-free stacked organic light emitting device with simplified pixel biasing. Adv. Mater. *11*, 907–910. https://doi.org/10.1002/(SICI)1521-4095(199908)11:11<907::AID-ADMA907>3.0.CO;2-L.

139. Ohisa, S., Kasuga, K., Endo, K., Pu, Y.-J., Chiba, T., and Kido, J. (2018). Operation behaviors of interconnecting-layers in solution-processed tandem organic light-emitting devices. Org. Electron. *63*, 98–103. https://doi.org/10.1016/j.orgel.2018.09.003.

140. Cui-Ran, C., Yu-Huan, C., Da-Shan, Q., Wei, Q., and Jin-Suo, L. (2010). Inverted bottom-emission organic light emitting diode using two n-doped layers for the enhanced performance. Chin. Phys. Lett. *27*, 117801.

https://doi.org/10.1088/0256-307X/27/11/117801.

141. Bansal, A.K., Sajjad, M.T., Antolini, F., Stroea, L., Gečys, P., Raciukaitis, G., André, P., Hirzer, A., Schmidt, V., and Ortolani, L. (2015). In situ formation and photo patterning of emissive quantum dots in small organic molecules. Nanoscale *7*, 11163–11172. https://doi.org/10.1039/C5NR01401H.

142. Mali, S.S., Dalavi, D., Bhosale, P., Betty, C., Chauhan, A., and Patil, P. (2012). Electro-optical properties of copper phthalocyanines (CuPc) vacuum deposited thin films. RSC Adv. *2*, 2100–2104. https://doi.org/10.1039/C2RA00670G.

143. Song, L., Hu, Y., Zhang, N., Li, Y., Lin, J., and Liu, X. (2016). Improved performance of organic light-emitting field-effect transistors by interfacial modification of hole-transport layer/emission layer: incorporating organic heterojunctions. ACS Appl. Mater. Interfaces *8*, 14063–14070. https://doi.org/10.1021/acsami.6b02618.

144. Karak, S., Ray, S., and Dhar, A. (2010). Improved photovoltaic properties of pentacene/n, n′-dioctyl-3, 4, 9, 10-perylenedicarboximide-based organic heterojunctions with thermal annealing. Sol. Energy Mater. Sol. Cells *94*, 836–841. https://doi.org/10.1016/j.solmat.2010.01.002.

145. Hung, L.S., and Tang, C.W. (1999). Interface engineering in preparation of organic surface-emitting diodes. Appl. Phys. Lett. *74*, 3209–3211. https://doi.org/10.1063/1.124107.

146. Parthasarathy, G., Adachi, C., Burrows, P.E., and Forrest, S.R. (2000). High-efficiency transparent organic light-emitting devices. Appl. Phys. Lett. *76*, 2128–2130. https://doi.org/10.1063/1.126275.

147. Dobbertin, T., Werner, O., Meyer, J., Kammoun, A., Schneider, D., Riedl, T., Becker, E., Johannes, H.-H., and Kowalsky, W. (2003). Inverted hybrid organic light-emitting device with polyethylene dioxythiophene-polystyrene sulfonate as an anode buffer layer. Appl. Phys. Lett. *83*, 5071–5073. https://doi.org/10.1063/1.1634688.

148. Kim, J.-B., Lee, J.-H., Moon, C.-K., Kim, S.-Y., and Kim, J.-J. (2013). Highly enhanced light extraction from surface plasmonic loss minimized organic light-emitting diodes. Adv. Mater. *25*, 3571–3577. https://doi.org/10.1002/adma.201205233.

149. Kim, J.-B., Lee, J.-H., Moon, C.-K., and Kim, J.-J. (2014). Highly efficient inverted top emitting organic light emitting diodes using a transparent top electrode with color stability on viewing angle. Appl. Phys. Lett. *104*, 073301. https://doi.org/10.1063/1.4865765.

150. Park, C.H., Lee, H.J., Hwang, J.H., Kim, K.N., Shim, Y.S., Jung, S.-G., Park, C.H., Park, Y.W., and Ju, B.-K. (2015). High-performance hybrid buffer layer using 1,4,5,8,9,11-hexaazatriphenylenehexacarbonitrile/molybdenum oxide in inverted top-emitting organic light-emitting diodes. ACS Appl. Mater. Interfaces *7*, 6047–6053. https://doi.org/10.1021/am5091066.

151. Duong, T., Lal, N., Grant, D., Jacobs, D., Zheng, P., Rahman, S., Shen, H., Stocks, M., Blakers, A., Weber, K., et al. (2016). Semitransparent perovskite solar cell with sputtered front and rear electrodes for a four-terminal tandem. IEEE J. Photovoltaics *6*, 679–687. https://doi.org/10.1109/JPHOTOV.2016.2521479.

152. Li, N., Meng, F., Huang, F., Yu, G., Wang, Z., Yan, J., Zhang, Y., Ai, Y., Shou, C., Zeng, Y., et al. (2020). Room-temperature sputtered aluminum-doped zinc oxide for semitransparent perovskite solar cells. ACS Appl. Energy Mater. *3*, 9610–9617. https://doi.org/10.1021/acsaem.0c01081.

153. George, S.M. (2010). Atomic layer deposition: an overview. Chem. Rev. *110*, 111–131. https://doi.org/10.1021/cr900056b.

154. Emslie, D.J., Chadha, P., and Price, J.S. (2013). Metal ALD and pulsed CVD: Fundamental reactions and links with solution chemistry. Coord. Chem. Rev. *257*, 3282–3296. https://doi.org/10.1016/j.ccr.2013.07.010.

155. Groner, M., Fabreguette, F., Elam, J., and George, S.M. (2004). Low-temperature Al2O3 atomic layer deposition. Chem. Mater. *16*, 639–645. https://doi.org/10.1021/cm0304546.

156. Yoon, K.H., Kim, H., Koo Lee, Y.-E., Shrestha, N.K., and Sung, M.M. (2017). UV-enhanced atomic layer deposition of Al2O3 thin films at low temperature for gas-diffusion barriers. RSC Adv. *7*, 5601–5609. https://doi.org/10.1039/C6RA27759D.

157. Palmstrom, A.F., Eperon, G.E., Leijtens, T., Prasanna, R., Habisreutinger, S.N., Nemeth, W., Gaulding, E.A., Dunfield, S.P., Reese, M., Nanayakkara, S., et al. (2019). Enabling flexible all-perovskite tandem solar cells. Joule *3*, 2193–2204. https://doi.org/10.1016/j.joule.2019.05.009.

158. Palmstrom, A.F., Raiford, J.A., Prasanna, R., Bush, K.A., Melany, S., Cheacharoen, R., Minichetti, M.C., Bergsman, D.S., Leijtens, T., Wang, H.-P., et al. (2018). Interfacial effects of tin oxide atomic layer deposition in metal halide perovskite photovoltaics. Adv. Energy Mater. *8*, 1800591. https://doi.org/10.1002/aenm.201800591.

159. Werner, J., Sahli, F., Fu, F., Diaz Leon, J.J., Walter, A., Kamino, B.A., Niesen, B., Nicolay, S., Jeangros, Q., and Ballif, C. (2018). Perovskite/perovskite/silicon monolithic triple-junction solar cells with a fully textured design. ACS Energy Lett. *3*, 2052–2058. https://doi.org/10.1021/acsenergylett.8b01165.

160. Chang, C.-Y., Lee, K.-T., Huang, W.-K., Siao, H.-Y., and Chang, Y.-C. (2015). High-performance, air-stable, low-temperature processed semitransparent perovskite solar cells enabled by atomic layer deposition. Chem. Mater. *27*, 5122–5130. https://doi.org/10.1021/acs.chemmater.5b01933.

161. Raiford, J., Belisle, R., Bush, K., Prasanna, R., Palmstrom, A., McGehee, M., and Bent, S. (2019). Atomic layer deposition of vanadium oxide to reduce parasitic absorption and improve stability in n-i-p perovskite solar cells for tandems. Sustain. Energ. Fuels *3*, 1517–1525. https://doi.org/10.1039/C9SE00081J.

162. Rajbhandari, P.P., and Dhakal, T.P. (2020). Low temperature ALD growth optimization of ZnO, TiO2, and Al2O3 to be used as a buffer layer in perovskite solar cells. J. Vacuum Sci. Technol. A Vacuum Surf. Films *38*, 032406. https://doi.org/10.1116/1.5139247.

163. Aydin, E., Liu, J., Ugur, E., Azmi, R., Harrison, G.T., Hou, Y., Chen, B., Zhumagali, S., De Bastiani, M., and Wang, M. (2021). Ligand-bridged charge extraction and enhanced quantum efficiency enable efficient nip perovskite/silicon tandem solar cells. Energy Environ. Sci. https://doi.org/10.1039/D1EE01206A.

164. Eom, T., Kim, S., Agbenyeke, R.E., Jung, H., Shin, S.M., Lee, Y.K., Kim, C.G., Chung, T.-M., Jeon, N.J., Park, H.H., and Seo, J. (2020). Copper oxide buffer layers by pulsed-chemical vapor deposition for semitransparent perovskite solar cells. Adv. Mater. Interfaces *8*, 2001482. https://doi.org/10.1002/admi.202001482.

165. Hong, H.K., Kim, I.Y., Shin, S.W., Song, G.Y., Cho, J.Y., Gang, M.G., Shin, J.C., Kim, J.H., and Heo, J. (2016). Atomic layer deposited zinc oxysulfide n-type buffer layers for Cu2ZnSn (S, Se) 4 thin film solar cells. Sol. Energy Mater. Sol. Cells *155*, 43–50. https://doi.org/10.1016/j.solmat.2016.04.054.

166. Schulze, P., Bett, A., Bivour, M., Caprioglio, P., Gerspacher, F., Kabakli, Ö., Richter, A., Stolterfoht, M., Zhang, Q., Neher, D., et al. (2020). 25.1% High-efficient monolithic perovskite silicon tandem solar cell with a high band gap perovskite absorber. Sol. RRL *4*, 200015. https://doi.org/10.1002/solr.202000152.

167. Mattinen, M., Wree, J.-L., Stegmann, N., Ciftyurek, E., Achhab, M.E., King, P.J., Mizohata, K., Räisänen, J., Schierbaum, K.D., Devi, A., et al. (2018). Atomic layer deposition of molybdenum and tungsten oxide thin films using heteroleptic Imido-Amidinato precursors: process development, film characterization, and gas sensing properties. Chem. Mater. *30*, 8690–8701. https://doi.org/10.1021/acs.chemmater.8b04129.

168. Prasadam, V.P., Bahlawane, N., Mattelaer, F., Rampelberg, G., Detavernier, C., Fang, L., Jiang, Y., Martens, K., Parkin, I.P., and Papakonstantinou, I. (2019). Atomic layer deposition of vanadium oxides: process and application review. Mater. Today Chem. *12*, 396–423. https://doi.org/10.1016/j.mtchem.2019.03.004.

169. Köhnen, E., Jošt, M., Morales, A.B., Tockhorn, P., Al-Ashouri, A., Macco, B., Kegelmann, L., Korte, L., Rech, B., Schlatmann, R., et al. (2019). Highly efficient monolithic perovskite silicon tandem solar cells: Analyzing the ınfluence of current mismatch on device performance. Sustain. Energ. Fuels *3*, 1995–2005. https://doi.org/10.1039/C9SE00120D.

170. Xu, J., Boyd, C.C., Yu, Z.J., Palmstrom, A.F., Witter, D.J., Larson, B.W., France, R.M., Werner, J., Harvey, S.P., Wolf, E.J., et al. (2020). Triple-halide wide–band gap perovskites with suppressed phase segregation for efficient tandems. Science *367*, 1097–1104. https://doi.org/10.1126/science.aaz5074.

171. Xiao, K., Lin, R., Han, Q., Hou, Y., Qin, Z., Nguyen, H.T., Wen, J., Wei, M., Yeddu, V., Saidaminov, M.I., et al. (2020). All-perovskite

tandem solar cells with 24.2% certified efficiency and area over 1 cm2 using surface-anchoring zwitterionic antioxidant. Nat. Energy *5*, 870–880. https://doi.org/10.1038/s41560-020-00705-5.

172. Brinkmann, K., Becker, T., Zimmermann, F., Gahlmann, T., Theisen, M., Haeger, T., Olthof, S., Kreusel, C., Günster, M., Maschwitz, T., et al. (2020). 23.5% efficient monolithic perovskite/organic tandem solar cells based on an ultra-thin metal-like metal-oxide interconnect. Res. Square Data. https://doi.org/10.21203/rs.3.rs-125381/v1.

173. Eperon, G.E., Leijtens, T., Bush, K.A., Prasanna, R., Green, T., Wang, J.T.-W., McMeekin, D.P., Volonakis, G., Milot, R.L., May, R., et al. (2016). Perovskite-perovskite tandem photovoltaics with optimized band gaps. Science *354*, 861–865. https://doi.org/10.1126/science.aaf9717.

174. Keum, C., Murawski, C., Archer, E., Kwon, S., Mischok, A., and Gather, M.C. (2020). A substrateless, flexible, and water-resistant organic light-emitting diode. Nat. Commun. *11*, 1–9. https://doi.org/10.1038/s41467-020-20016-3.

175. Kaya, I.C., Zanoni, K.P., Palazon, F., Sessolo, M., Akyildiz, H., Sonmezoglu, S., and Bolink, H.J. (2021). Crystal reorientation and amorphization ınduced by stressing efficient and stable p–ı–n vacuum-processed MAPbI3 perovskite solar cells. Adv. Energy Sustain. Res. *2*, 2000065. https://doi.org/10.1002/aesr.202000065.

176. Raninga, R.D., Jagt, R.A., Béchu, S., Huq, T.N., Li, W., Nikolka, M., Lin, Y.-H., Sun, M., Li, Z., Li, W., et al. (2020). Strong performance enhancement in lead-halide perovskite solar cells through rapid, atmospheric deposition of n-type buffer layer oxides. Nano Energy *75*, 104946. https://doi.org/10.1016/j.nanoen.2020.104946.

177. Sinha, S., Nandi, D.K., Pawar, P.S., Kim, S.-H., and Heo, J. (2020). A review on atomic layer deposited buffer layers for Cu(In, Ga)Se2 (CIGS) thin film solar cells: past, present, and future. Sol. Energy *209*, 515–537. https://doi.org/10.1016/j.solener.2020.09.022.

178. Bett, A.J., Winkler, K.M., Bivour, M., Cojocaru, L., Kabakli, Ö.Ş., Schulze, P.S.C., Siefer, G., Tutsch, L., Hermle, M., Glunz, S.W., and Goldschmidt, J.C. (2019). Semi-transparent perovskite solar cells with ITO directly sputtered on Spiro-OMeTAD for tandem applications. ACS Appl. Mater. Interfaces *11*, 45796–45804. https://doi.org/10.1021/acsami.9b17241.

179. Lei, H., Ichikawa, K., Hoshi, Y., Wang, M., Uchida, T., and Sawada, Y. (2010). A study of deposition of ITO films on organic layer using facing target sputtering in Ar and Kr gases. Thin Solid Films *518*, 2926–2929. https://doi.org/10.1016/j.tsf.2009.08.059.

180. Hamaguchi, D., Kobayashi, S.-i., Uchida, T., Sawada, Y., Lei, H., and Hoshi, Y. (2016). Improvement in luminance efficiency of organic light emitting diodes by suppression of secondary electron bombardment of substrate during sputter deposition of top electrode films. Jpn. J. Appl. Phys. *55*, 106501. https://doi.org/10.7567/jjap.55.106501.

181. Lim, S.-H., Seok, H.-J., Kwak, M.-J., Choi, D.-H., Kim, S.-K., Kim, D.-H., and Kim, H.-K. (2021). Semi-transparent perovskite solar cells with bidirectional transparent electrodes. Nano Energy *82*, 105703. https://doi.org/10.1016/j.nanoen.2020.105703.

182. Ramos, F.J., Jutteau, S., Posada, J., Bercegol, A., Rebai, A., Guillemot, T., Bodeux, R., Schneider, N., Loones, N., Ory, D., et al. (2018). Highly efficient MoOx-free semitransparent perovskite cell for 4 T tandem application improving the efficiency of commercially-available Al-BSF silicon. Sci. Rep. *8*, 16139. https://doi.org/10.1038/s41598-018-34432-5.

183. Depla, D., Buyle, G., Haemers, J., and De Gryse, R. (2006). Discharge voltage measurements during magnetron sputtering. Surf. Coat. Technol. *200*, 4329–4338. https://doi.org/10.1016/j.surfcoat.2005.02.166.

184. Bender, M., Trube, J., and Stollenwerk, J. (1999). Characterization of a RF/DC magnetron discharge for the sputter deposition of transparent and highly conductive ITO films. Appl. Phys. A. *69*, 397–401. https://doi.org/10.1007/s003390051021.

185. Bikowski, A., Welzel, T., and Ellmer, K. (2013). The impact of negative oxygen ion bombardment on electronic and structural properties of magnetron sputtered ZnO:Al films. Appl. Phys. Lett. *102*, 242106. https://doi.org/10.1063/1.4811647.

186. Kim, S., and Kim, K.H. (2020). Effect of magnetic field arrangement of facing targets sputtering (FTS) system on controlling plasma confinement. Coatings *10*, 321. https://doi.org/10.3390/coatings10040321.

187. Takeda, H., Sato, Y., Iwabuchi, Y., Yoshikawa, M., and Shigesato, Y. (2009). Electrical and optical properties of Al-doped ZnO films deposited by hollow cathode gas flow sputtering. Thin Solid Films *517*, 3048–3052. https://doi.org/10.1016/j.tsf.2008.11.114.

188. Nanto, H., Minami, T., Shooji, S., and Takata, S. (1984). Electrical and optical properties of zinc oxide thin films prepared by rf magnetron sputtering for transparent electrode applications. J. Appl. Phys. *55*, 1029–1034. https://doi.org/10.1063/1.333196.

189. Yamaguchi, T., Tanaka, T., and Yoshida, A. (2002). Effect of substrate position in i-ZnO thin-film formation to Cu(In,Ga)Se2 solar cell. J. Vacuum Sci. Technol. A *20*, 1755–1758. https://doi.org/10.1116/1.1502696.

190. Yasuda, Y., Kobayashi, S.-i., Uchida, T., and Hoshi, Y. (2020). Top-emission organic light emitting diode with indium tin oxide top-electrode films deposited by a low-damage facing-target type sputtering method. Thin Solid Films *698*, 137868. https://doi.org/10.1016/j.tsf.2020.137868.

191. Jeong, J.-A., and Kim, H.-K. (2013). Al2O3/Ag/Al2O3 multilayer thin film passivation prepared by plasma damage-free linear facing target sputtering for organic light emitting diodes. Thin Solid Films *547*, 63–67. https://doi.org/10.1016/j.tsf.2013.05.003.

192. Kim, H.Y., Park, Y.J., Kim, J., Han, C.J., Lee, J., Kim, Y., Greco, T., Ippen, C., Wedel, A., and Ju, B.K. (2016). Transparent InP quantum dot light-emitting diodes with ZrO2 electron transport layer and ındium zinc oxide top electrode. Adv. Funct. Mater. *26*, 3454–3461. https://doi.org/10.1002/adfm.201505549.

193. Görrn, P., Sander, M., Meyer, J., Kröger, M., Becker, E., Johannes, H.H., Kowalsky, W., and Riedl, T. (2006). Towards see-through displays: fully transparent thin-film transistors driving transparent organic light-emitting diodes. Adv. Mater. *18*, 738–741. https://doi.org/10.1002/adma.200501957.

194. Onai, Y., Uchida, T., Kasahara, Y., Ichikawa, K., and Hoshi, Y. (2008). Transparent conductive film for top-emission organic light-emitting devices by low damage facing target sputtering. Thin Solid Films *516*, 5911–5915. https://doi.org/10.1016/j.tsf.2007.10.043.

195. Zhou, Z., Zhang, Y., Chen, X., Li, S., Zhao, Y., and Zhang, X. (2020). Innovative wide-spectrum Mg and Ga-codoped ZnO transparent conductive films grown via reactive plasma deposition for si heterojunction solar cells. ACS Appl. Energy Mater. *3*, 1574–1584. https://doi.org/10.1021/acsaem.9b02064.

196. Lu, Z., Meng, F., Cui, Y., Shi, J., Feng, Z., and Liu, Z. (2013). High quality of IWO films prepared at room temperature by reactive plasma deposition for photovoltaic devices. J. Phys. D Appl. Phys. *46*, 075103. https://doi.org/10.1088/0022-3727/46/7/075103.

197. Lucas, B., Rammal, W., and Moliton, A. (2006). ITO films realized at room-temperature by ion beam sputtering for high-performance flexible organic light-emitting diodes. EPJ Appl. Phys. *34*, 179–187. https://doi.org/10.1051/epjap:2006056.

198. Prakash, S. (2008). P-224: damage-free cathode coating process for OLEDs. SID Symp. Dig. Tech. Pap. *39*, 2046–2048. https://doi.org/10.1889/1.3069605.

199. Lim, J., Jeong, C., Vozny, A., Lee, J., Kim, M., and Yeom, G. (2007). Top-emitting organic light-emitting diode using transparent conducting indium oxide layer fabricated by a two-step ion beam-assisted deposition. Surf. Coat. Technol. *201*, 5358–5362. https://doi.org/10.1016/j.surfcoat.2006.07.036.

200. Smirnov, Y., Schmengler, L., Kuik, R., Repecaud, P.-A., Najafi, M., Zhang, D., Theelen, M., Aydin, E., Veenstra, S., De Wolf, S., and Morales-Masis, M. (2021). Scalable pulsed laser deposition of transparent rear electrode for perovskite solar cells. Adv. Mater. Technol. *6*, 2000856. https://doi.org/10.1002/admt.202000856.

201. Schubert, S., Schmidt, F., von Wenckstern, H., Grundmann, M., Leo, K., and Müller-Meskamp, L. (2015). Eclipse pulsed laser deposition for damage-free preparation of transparent ZnO electrodes on top of organic solar cells. Adv. Funct. Mater. *25*, 4321–4327. https://doi.org/10.1002/adfm.201500569.

202. Meyer, J., Görrn, P., Hamwi, S., Johannes, H.-H., Riedl, T., and Kowalsky, W. (2008). Indium-free transparent organic light emitting diodes with Al doped ZnO electrodes grown by atomic layer and pulsed laser deposition. Appl. Phys. Lett. *93*, 073308. https://doi.org/10.1063/1.2975176.

203. Matsubara, K., Fons, P., Iwata, K., Yamada, A., Sakurai, K., Tampo, H., and Niki, S. (2003). ZnO transparent conducting films deposited by pulsed laser deposition for solar cell applications. Thin Solid Films *431*, 369–372. https://doi.org/10.1016/S0040-6090(03)00243-8.

204. Illiberi, A., Scherpenborg, R., Wu, Y., Roozeboom, F., and Poodt, P. (2013). Spatial atmospheric atomic layer deposition of AlxZn1–xO. ACS Appl. Mater. Interfaces *5*, 13124–13128. https://doi.org/10.1021/am404137e.

205. Illiberi, A., Scherpenborg, R., Roozeboom, F., and Poodt, P. (2014). Atmospheric spatial atomic layer deposition of In-doped ZnO. ECS J. Solid State Sci. Technol. *3*, 111–114. https://doi.org/10.1149/2.002405jss.

206. Kuang, Y., Macco, B., Karasulu, B., Ande, C.K., Bronsveld, P.C., Verheijen, M.A., Wu, Y., Kessels, W.M., and Schropp, R.E. (2017). Towards the implementation of atomic layer deposited In2O3: H in silicon heterojunction solar cells. Sol. Energy Mater. Sol. Cells *163*, 43–50. https://doi.org/10.1016/j.solmat.2017.01.011.

207. Favier, A., Muñoz, D., De Nicolás, S.M., and Ribeyron, P.-J. (2011). Boron-doped zinc oxide layers grown by metal-organic CVD for silicon heterojunction solar cells applications. Sol. Energy Mater. Sol. Cells *95*, 1057–1061. https://doi.org/10.1016/j.solmat.2010.11.013.